Kinematics Modeling and Control of Spherical Rolling Contact Joint and Manipulator

Lijun Zong, *Member, IEEE*, Guanqi Liang, *Student Member, IEEE*, and Tin Lun Lam, *Senior Member, IEEE*

***Abstract*—Rolling contact joints are attracting increasing interest in applications to robotic fingers and manipulators, due to the potential of the absence of abrasion wear, the simplification of the controller, and the enlargement of reachable configurations. This article first proposes a novel two-degree-of-freedom (DOF) spherical rolling contact (SRC) joint, with the joint model elements being formulated, including *rotation matrix*, *position vector*, and *free modes*, as with those of classic joints. As an application, a new kind of serial manipulator formed by the SRC joints is presented, and its forward and inverse kinematics are modeled. The motions of the two-DOF SRC joint and manipulator are implemented using the FreeBOT, and the control method is proposed for the FreeBOT, such that the SRC joint and manipulator realize the motion control. The kinematics and control of the two-DOF SRC joint and manipulator are validated using physics simulations and on a real manipulator formed by FreeBOTs.**

***Index Terms*—Forward kinematics, inverse kinematics (IK), manipulator, modular self-reconfigurable robot, rolling contact (RC) joint.**

NOMENCLATURE

B_i	Links of the manipulator.
$\boldsymbol{J}_{B_n}$	Jacobian matrix of the SRC joint manipulator.
$\boldsymbol{K}_p$	End-effector position control gain.
$\boldsymbol{K}_a$	End-effector orientation control gain.
k_{φ_i}	*Steering* control gain of the driving trolley i.
k_{s_i}	*Forward* control gain of the driving trolley i.
l_i	Radius of the sphere body B_i (m).
$l_{i,w}$	Wheel interval of the driving trolley i (m).
n	Number of joints.
P_i	Virtual tangent plane between B_i and B_{i-1}.
$\boldsymbol{q}_i$	Unit quaternion that represents the orientation of B_i with respect to B_{i-1}.
$\boldsymbol{q}_{i,1}$	Unit quaternion that represents the orientation of B_i with respect to P_i.
$\boldsymbol{q}_{i-1,2}$	Unit quaternion that represents the orientation of B_{i-1} with respect to P_i.
${}^{*}\boldsymbol{R}_{\#}$	Rotation matrix of body $\#$ relative to body $*$.
${}^{*}_{**}\boldsymbol{r}_{\#}$	Position of body $\#$ with respect to $*$ and expressed in the frame $**$ (m).
$r_{i,w}$	Wheel radius of the driving trolley i (m).
$r_{i,\text{out}}$	Outer radius of the FreeBOT shell (m).
$r_{i,\text{in}}$	Inner radius of the FreeBOT shell (m).
r	Right superscript that represents reference values.
s_i	*Forward* arc distance of the driving trolley i (m).
u_{if}	*Forward* speed of the driving trolley i (m/s).
u_{is}	*Steering* speed of the driving trolley i (rad/s).
w_{ir}	Rotation speed of the right wheel (rad/s).
w_{il}	Rotation speed of the left wheel (rad/s).
$\boldsymbol{\Phi}_i$	Free-mode matrix of the SRC joint i.
${}^{*}_{**}\boldsymbol{v}_{\#}$	Linear velocity of body $\#$ with respect to $*$ and expressed in the frame $**$ (m/s).
${}^{*}_{**}\boldsymbol{\omega}_{\#}$	Angular velocity of body $\#$ with respect to $*$ and expressed in the frame $**$ (rad/s).
$\boldsymbol{\omega}$	SRC joint velocity set of the manipulator (rad/s).
φ_i	*Steering* angle of the driving trolley i (rad).
η_i	Scalar part of the unit quaternion $\boldsymbol{q}_i$.
$\boldsymbol{\epsilon}_i$,	Vector part of the unit quaternion $\boldsymbol{q}_i$.
$\Delta\theta_{i,1}\hat{\boldsymbol{e}}_{i,1}$	B_i rotates through the angle $\Delta\theta_{i,1}$ around the unit axis $\hat{\boldsymbol{e}}_{i,1}$ relative to P_i.
$\Delta\theta_{i-1,2}\hat{\boldsymbol{e}}_{i-1,2}$	B_{i-1} rotates through the angle $\Delta\theta_{i-1,2}$ around the unit axis $\hat{\boldsymbol{e}}_{i-1,2}$ relative to P_i.
$\times$	Cross product of two vectors.
$\widetilde{\square}$	Conjugate of a quaternion.

Manuscript received 21 December 2021; revised 19 May 2022; accepted 7 July 2022. Date of publication 17 August 2022; date of current version 8 February 2023. This work was supported in part by the National Natural Science Foundation of China under Grant 62073274 and in part by the Shenzhen Institute of Artificial Intelligence and Robotics for Society under Grant AC01202101103. This paper was recommended for publication by Associate Editor S. Briot and Editor M. Yim upon evaluation of the reviewers' comments. *(Corresponding author: Tin Lun Lam.)*

Lijun Zong is with the Institute of Robotics and Intelligent Manufacturing, The Chinese University of Hong Kong, Shenzhen 518172, China, and also with the University of Science and Technology of China, Hefei 230026, China (e-mail: zonglijun@mail.nwpu.edu.cn).

Guanqi Liang and Tin Lun Lam are with the Shenzhen Institute of Artificial Intelligence and Robotics for Society and the School of Science and Engineering, The Chinese University of Hong Kong, Shenzhen 518172, China (e-mail: guanqiliang@link.cuhk.edu.cn; tllam@cuhk.edu.cn).

Color versions of one or more figures in this article are available at https://doi.org/10.1109/TRO.2022.3190790.

Digital Object Identifier 10.1109/TRO.2022.3190790

I. INTRODUCTION

ROLLING contact (RC) in which one body rolls without slipping over the surface of the other is widespread in robotics, such as spherical robots [1], multifingered robotic hands [2], [3], and manipulator joints [4], [5]. When forming an RC joint, it has the advantages of the absence of abrasion wear, the simplification of the controller design, and the enlargement of reachable configurations due to the nature of nonholonomic constraints [3], [6]. Research on a single joint having multiple degrees of freedom (DOFs) that can be actuated has been ongoing, which will make the robots smaller, less costly, or more

functional than conventional robots [7]. No work has proposed multi-DOF RC joints, let alone investigated the associated joint modeling, implementation, and applications.

RC actually encompasses several different geometries, for example, sphere on a plane or on another sphere. Hence, the RC pair allows relative motions with different dimensions, forming an RC kinematic joint with one, two, or three DOFs [8]. Regardless of the number of DOFs, the no-slip condition associated with RC, as a nonholonomic constraint [8], represents the principle basis of its kinematics modeling, which requires the instantaneous relative velocity between the contact points on the two bodies be zero. Li and Canny [6] review the geometries of contact surfaces and the kinematics of contact. Using a Darboux frame, the kinematics of spin-rolling contact motion are studied in [3], [9], and [10]. These works provide alternative ways of describing RC motion in a general sense, which are inspirational for formulating the RC joint model.

RC joints are attracting increasing attention on their potential applications to robotic fingers [11]–[16], manipulator [4], [5], [17]–[22], etc. The kinematics of the one-DOF circular rolling contact (CRC) joint is modeled in [11], which is used to form a two-joint robot finger. To improve the compliance of the robotic hands, RC joints have been adopted to manufacture sophisticated fingers [12]–[14]. The optimal design of underactuated fingers and hand implant using an RC joint is studied to increase performance in robotic and prosthetic hand applications [15], [16]. A three-DOF serial chain [17] and a three-DOF planar parallel mechanism [4] using CRC joints are designed, respectively, with the forward kinematics and inverse kinematics (IK) being analyzed. Contributing to the compactness, miniaturization potential, and lower part count, the RC joints are used to construct hyper-redundant manipulators for minimally invasive surgery [5], [19], [20], with the performance of the RC joints in terms of payload, force, and stiffness being continuously optimized [18], [21], [22]. It is worth noting that so far only one-DOF CRC joint has been explored, and the robotic fingers and manipulators perform only planar motions. To the authors' knowledge, there is only one work, inspired by human knee anatomy, considering using coupled spheres rather than cylinders to form an RC joint for usage as a knee joint in lower limb exoskeletons [23]. However, the formed RC joint is not specifically studied, whose kinematics are equivalently simulated using those of multiple combined revolute joints. A one-DOF RC pair that can generate spatial relative motion between links is proposed in [24]–[26]; however, the allowed spatial rolling motion needs to be prespecified; then, the shapes of both the pairing elements that can generate the specified rolling motions must be manufactured.

This article first proposes a two-DOF spherical rolling contact (SRC) joint. The two-DOF SRC joint is formed by relative rolling motions about two axes on the common tangent plane of the two sphere shells that may have different radii. The joint model of the two-DOF SRC joint is formulated in this article, which includes *rotation matrix*, *position vector*, and *free modes*, as with those summarized for classic joints, for example, revolute joint [8]. Using the proposed two-DOF SRC joints, a new kind of serial manipulator is presented, whose forward kinematics and IK modeling is performed using the two-DOF SRC joint model. Owing to the geometric symmetry of the spherical units, the SRC joint manipulator has the advantage of performing tasks in environments with obstacles or narrow spaces.

The FreeBOT is used to implement the motions of the two-DOF SRC joint and manipulator [27], where a driving trolley moves forward and steers inside the spherical iron shell to drive the joint motions, and a magnet at trolley's bottom attracts the other body not to separate. This article also develops a physics simulation system for the proposed SRC joint and manipulator and builds a real SRC joint manipulator using FreeBOTs, such that the two-DOF SRC joint model, manipulator kinematics, and control method can be validated.

The main contributions of this article are threefold.

1) A new kind of robotic joint, termed as two-DOF SRC joint, is proposed; the joint model is formulated as with its other classic joint counterparts.
2) A new kind of serial manipulator composed of the SRC joints is presented, whose forward kinematics and IK are modeled.
3) The motion control of the two-DOF SRC joint and manipulator is realized using FreeBOT, which provides an alternative way for actively actuating the two-DOF SRC joint.

The rest of this article is organized as follows. Section II formulates the two-DOF SRC joint model. Section III derives the forward kinematics and IK model of the SRC joint manipulator. Section IV uses the FreeBOT to implement the motion control of the two-DOF SRC joint and manipulator. Section V validates the proposed two-DOF SRC joint model and the performance of the SRC joint manipulator with physics simulation and physical experiments, respectively. Finally, Section VI concludes this article.

II. SRC Joint

An RC joint is formed when one body *rolls without slipping* over the surface of the other [8]. As shown in Fig. 1, this article introduces a novel two-DOF SRC joint, including its *rotation matrix*, *position vector*, and *free modes*, which connects two spherical bodies that may have different geometric sizes.

The SRC joint provides two key constraints that combine to form a two-DOF joint. The first constraint ensures that the bodies do not separate at the point of contact. The second constraint is *rolling without slipping* about two axes on the common tangent plane between the two bodies.

As shown in Fig. 1, this article represents the bodies through their body-fixed frames $\sum B_i$ and $\sum B_{i-1}$ located at the sphere centers, with their radii denoted as l_i and l_{i-1}, respectively, such that $l_i \neq l_{i-1}$ is possible. For ease of joint modeling derivation, we introduce the virtual common tangent plane P_i between the bodies and its body-fixed frame $\sum P_i$ located at the point of contact of the two bodies. Supposing that the two-DOF SRC joint axes are aligned with the $\hat{x}$ and $\hat{y}$ axes of the frame $\sum P_i$, the initial joint state corresponds to the fact that $\sum B_i$, $\sum B_{i-1}$, and $\sum P_i$ have the same orientation.

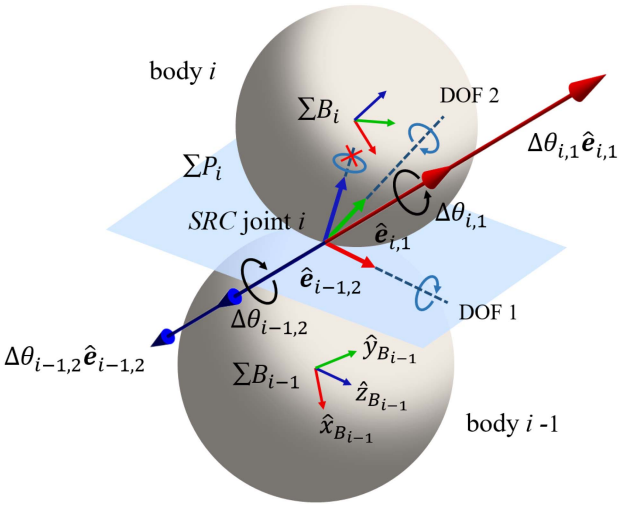

Fig. 1. Notations of the two-DOF SRC joint and its angle–axis orientation representation.

A. Rotation Matrix

The *rotation matrix* of the SRC joint transforms a vector expressed in frame $\sum B_i$ to a vector expressed in frame $\sum B_{i-1}$, which represents the orientation of frame $\sum B_i$ relative to frame $\sum B_{i-1}$. There are different ways for the representation of the orientation [8], such as Euler angles, angle–axis, and quaternions, which can be used to equivalently calculate the rotation matrix.

This article uses unit quaternion to describe the orientation of the body B_i with respect to the body B_{i-1}, denoted as $\boldsymbol{q}_i = [\eta_i, \boldsymbol{\epsilon}_i]^\top \in \mathbb{R}^4$, with η_i and $\boldsymbol{\epsilon}_i$ being the scalar and vector parts of the quaternion, respectively.

Defining the SRC joint velocity ${}^{B_{i-1}}_{P_i}\boldsymbol{\omega}_{B_i}$, which represents the angular velocity of $\sum B_i$ with respect to $\sum B_{i-1}$ and expressed in the frame $\sum P_i$ (note that the SRC joint axes are aligned with the axes of the frame $\sum P_i$), how the SRC joint velocity ${}^{B_{i-1}}_{P_i}\boldsymbol{\omega}_{B_i}$ makes the rotation matrix ${}^{B_{i-1}}\boldsymbol{R}_{B_i}$ change is the focus of this subsection. A more physically meaningful set of angular velocities ${}^{P_i}_{P_i}\boldsymbol{\omega}_{B_i}$ that closely relate to the driving unit of the SRC joint, as shown in Section IV-A, is defined; it has the following relationship with ${}^{B_{i-1}}_{P_i}\boldsymbol{\omega}_{B_i}$:

$$ {}^{B_{i-1}}_{P_i}\boldsymbol{\omega}_{B_i} = \frac{l_i + l_{i-1}}{l_i} {}^{P_i}_{P_i}\boldsymbol{\omega}_{B_i}. \tag{1} $$

Defining the unit quaternion $\boldsymbol{q}_{i,1} = [\eta_{i,1}, \boldsymbol{\epsilon}_{i,1}]^\top \in \mathbb{R}^4$ to represent the orientation of the body B_i with respect to the tangent plane P_i, its derivative can be calculated from ${}^{P_i}_{P_i}\boldsymbol{\omega}_{B_i}$ as

$$ \begin{cases} \dot{\eta}_{i,1} = -\frac{1}{2} {}^{P_i}_{P_i}\boldsymbol{\omega}_{B_i}^\top \boldsymbol{\epsilon}_{i,1} \\ \dot{\boldsymbol{\epsilon}}_{i,1} = \frac{1}{2}\left(\eta_{i,1} {}^{P_i}_{P_i}\boldsymbol{\omega}_{B_i} - \boldsymbol{\epsilon}_{i,1} \times {}^{P_i}_{P_i}\boldsymbol{\omega}_{B_i}\right) \end{cases} \tag{2} $$

where "$\times$" represents the cross product.

The unit quaternion $\boldsymbol{q}_{i,1}$ is obtained by integrating over (2). In order to calculate $\boldsymbol{q}_i$ from $\boldsymbol{q}_{i,1}$, we define the unit quaternion $\boldsymbol{q}_{i-1,2} = [\eta_{i-1,2}, \boldsymbol{\epsilon}_{i-1,2}]^\top \in \mathbb{R}^4$ to represent the orientation of $\sum B_{i-1}$ relative to $\sum P_i$ and first establish the relationship between the angular displacements of $\sum B_i$ and $\sum B_{i-1}$ relative to $\sum P_i$ as follows. The angle–axis representations of angular displacement of $\sum B_i$ and $\sum B_{i-1}$ relative to the $\sum P_i$, denoted as $\Delta\theta_{i,1}\hat{\boldsymbol{e}}_{i,1}$ and $\Delta\theta_{i-1,2}\hat{\boldsymbol{e}}_{i-1,2}$, are presented in Fig. 1, where frames $\sum B_i$ and $\sum B_{i-1}$ rotate through the angles $\Delta\theta_{i,1}$ and $\Delta\theta_{i-1,2}$ about an axis defined by the unit vector $\hat{\boldsymbol{e}}_{i,1}$ and $\hat{\boldsymbol{e}}_{i-1,2}$ relative to frame $\sum P_i$, respectively. The following relationships exist between $\Delta\theta_{i,1}\hat{\boldsymbol{e}}_{i,1}$ and $\Delta\theta_{i-1,2}\hat{\boldsymbol{e}}_{i-1,2}$ according to the relativity principle in motion and *rolling without slipping* condition between the two sphere bodies

$$ \hat{\boldsymbol{e}}_{i-1,2} = -\hat{\boldsymbol{e}}_{i,1} \tag{3} $$

and (refer to Appendix A1)

$$ l_i\dot{\theta}_{i-1,2} = l_{i-1}\dot{\theta}_{i,1}. \tag{4} $$

The relationships (3) and (4) result in

$$ \Delta\theta_{i-1,2}\hat{\boldsymbol{e}}_{i-1,2} = -\frac{l_{i-1}}{l_i}\Delta\theta_{i,1}\hat{\boldsymbol{e}}_{i,1}. \tag{5} $$

Note that $\Delta\theta_{i,1}\hat{\boldsymbol{e}}_{i,1}$ and $\Delta\theta_{i-1,2}\hat{\boldsymbol{e}}_{i-1,2}$ can actually be viewed as a geometric representation of $\Delta\boldsymbol{q}_{i,1}$ and $\Delta\boldsymbol{q}_{i-1,2}$ [8], where $\Delta\boldsymbol{q}_{i,1} = \boldsymbol{q}_{i,1}(t)\widetilde{\boldsymbol{q}}_{i,1}(t_0)$ is the angular displacement calculated with quaternions, similar for $\Delta\boldsymbol{q}_{i-1,2}$, and the symbol "$\widetilde{\square}$" represents the conjugate of a quaternion. Therefore, given initial states $\boldsymbol{q}_{i,1}(t_0)$ and $\boldsymbol{q}_{i,1}(t)$ integrated over (2), $\Delta\boldsymbol{q}_{i,1}$ can be calculated and converted to $\Delta\theta_{i,1}\hat{\boldsymbol{e}}_{i,1}$. Then, $\Delta\theta_{i-1,2}\hat{\boldsymbol{e}}_{i-1,2}$ is calculated from $\Delta\theta_{i,1}\hat{\boldsymbol{e}}_{i,1}$ using (5) and converted back to $\Delta\boldsymbol{q}_{i-1,2}$ and then calculates $\boldsymbol{q}_{i-1,2}(t)$ (the conversions between the angle–axis representation and quaternion refer to Appendix A2).

So far, the orientations of the bodies $\sum B_i$ and $\sum B_{i-1}$, with respect to the tangent plane $\sum P_i$, represented by $\boldsymbol{q}_{i,1}$ and $\boldsymbol{q}_{i-1,2}$, have been obtained, and the orientation of $\sum B_i$ relative to $\sum B_{i-1}$, denoted as $\boldsymbol{q}_i$, can be calculated as

$$ \boldsymbol{q}_i = \widetilde{\boldsymbol{q}}_{i-1,2}\boldsymbol{q}_{i,1}. \tag{6} $$

Correspondingly, the rotation matrix of the SRC joint ${}^{B_{i-1}}\boldsymbol{R}_{B_i}$ can be calculated from the unit quaternion $\boldsymbol{q}_i$, as shown in Appendix A3.

B. Position Vector

The position vector of the SRC joint is defined as the translations from the origin of body $\sum B_{i-1}$ to the origin of body $\sum B_i$ along the SRC joint axes.

As shown in Fig. 1, the position vector of the SRC joint can be expressed as

$$ {}^{B_{i-1}}_{P_i}\boldsymbol{r}_{B_i} = \begin{bmatrix} 0 \\ 0 \\ l_i + l_{i-1} \end{bmatrix}. \tag{7} $$

C. Free Modes

The free modes of the SRC joint define the directions in which the motion of $\sum B_i$ relative to $\sum B_{i-1}$ is allowed. They are represented by the $6 \times n_i$ matrix $\boldsymbol{\Phi}_i$, whose columns are the Plücker coordinates of the allowable motion [8]; $n_i = 2$ is the number of SRC joint DOFs. Defining the spatial velocity

vector of $\sum B_i$, i.e., ${}^{B_{i-1}}_{B_{i-1}}\boldsymbol{\nu}_{B_i} = [{}^{B_{i-1}}_{B_{i-1}}\boldsymbol{\omega}^\top_{B_i}, {}^{B_{i-1}}_{B_{i-1}}\boldsymbol{v}^\top_{B_i}]^\top$, the matrix $\boldsymbol{\Phi}_i$ relates the spatial velocity vector ${}^{B_{i-1}}_{B_{i-1}}\boldsymbol{\nu}_{B_i}$ to the SRC joint velocities ${}^{B_{i-1}}_{P_i}\omega_{B_{ix}}$ and ${}^{B_{i-1}}_{P_i}\omega_{B_{iy}}$ (note that the rotation about the vertical axis of the tangent plane P_i between the bodies is not allowed, i.e., ${}^{B_{i-1}}_{P_i}\omega_{B_{iz}} = 0$)

$$ {}^{B_{i-1}}_{B_{i-1}}\boldsymbol{\nu}_{B_i} = \boldsymbol{\Phi}_i \begin{bmatrix} {}^{B_{i-1}}_{P_i}\omega_{B_{ix}} \\ {}^{B_{i-1}}_{P_i}\omega_{B_{iy}} \end{bmatrix}. \tag{8} $$

The angular velocities ${}^{B_{i-1}}_{B_{i-1}}\boldsymbol{\omega}_{B_i}$ and ${}^{B_{i-1}}_{P_i}\boldsymbol{\omega}_{B_i}$ satisfy the relationship

$$ {}^{B_{i-1}}_{B_{i-1}}\boldsymbol{\omega}_{B_i} = {}^{B_{i-1}}\boldsymbol{R}_{P_i}\, {}^{B_{i-1}}_{P_i}\boldsymbol{\omega}_{B_i}. \tag{9} $$

Given the unit quaternion $\boldsymbol{q}_{i\text{–}1,2}$ in Section II-A, the rotation matrix ${}^{B_{i-1}}\boldsymbol{R}_{P_i}$ is obtained from $\boldsymbol{q}_{i\text{–}1,2}$

$$ {}^{B_{i-1}}\boldsymbol{R}_{P_i} = \begin{bmatrix} \boldsymbol{f}_1(\boldsymbol{q}_{i\text{–}1,2}) & \boldsymbol{f}_2(\boldsymbol{q}_{i\text{–}1,2}) & \boldsymbol{f}_3(\boldsymbol{q}_{i\text{–}1,2}) \end{bmatrix} \tag{10} $$

where the expressions of the functions $\boldsymbol{f}_i$ refer to Appendix A3.

Substituting (10) into (9) results in

$$ {}^{B_{i-1}}_{B_{i-1}}\boldsymbol{\omega}_{B_i} = \begin{bmatrix} \boldsymbol{f}_1(\boldsymbol{q}_{i\text{–}1,2}) & \boldsymbol{f}_2(\boldsymbol{q}_{i\text{–}1,2}) \end{bmatrix} \begin{bmatrix} {}^{B_{i-1}}_{P_i}\omega_{B_{ix}} \\ {}^{B_{i-1}}_{P_i}\omega_{B_{iy}} \end{bmatrix}. \tag{11} $$

Therefore, we obtain the angular free-mode matrix $\boldsymbol{\Phi}_{i\boldsymbol{w}} = [\boldsymbol{f}_1(\boldsymbol{q}_{i\text{–}1,2}),\ \boldsymbol{f}_2(\boldsymbol{q}_{i\text{–}1,2})]$ that describes the generated angular motion of $\sum B_i$ relative to $\sum B_{i\text{–}1}$ when an SRC joint velocity is given.

The linear velocity ${}^{B_{i-1}}_{B_{i-1}}\boldsymbol{v}_{B_i}$ is calculated as (a more detailed derivation refers to Appendix A4)

$$ {}^{B_{i-1}}_{B_{i-1}}\boldsymbol{v}_{B_i} = (l_i + l_{i\text{–}1})\boldsymbol{f}_3^{\times}(\boldsymbol{q}_{i\text{–}1,2}) \left({}^{P_i}_{B_{i-1}}\boldsymbol{\omega}_{B_{i-1}} \right) \tag{12} $$

where $\boldsymbol{f}_3^{\times}(\boldsymbol{q}_{i\text{–}1,2})$ is the skew-symmetric matrix of $\boldsymbol{f}_3(\boldsymbol{q}_{i\text{–}1,2})$.

Similar to the SRC joint velocity relationship in (1), one has

$$ {}^{B_{i-1}}_{B_{i-1}}\boldsymbol{\omega}_{B_i} = -\frac{l_i + l_{i\text{–}1}}{l_{i\text{–}1}} {}^{P_i}_{B_{i-1}}\boldsymbol{\omega}_{B_{i-1}} \tag{13} $$

which makes (12) be

$$ {}^{B_{i-1}}_{B_{i-1}}\boldsymbol{v}_{B_i} = -l_{i\text{–}1}\boldsymbol{f}_3^{\times}(\boldsymbol{q}_{i\text{–}1,2}) {}^{B_{i-1}}_{B_{i-1}}\boldsymbol{\omega}_{B_i}. \tag{14} $$

Using (11), (14) turns into

$$ {}^{B_{i-1}}_{B_{i-1}}\boldsymbol{v}_{B_i} = -l_{i\text{–}1} \begin{bmatrix} \boldsymbol{f}_3^{\times}\boldsymbol{f}_1(\boldsymbol{q}_{i\text{–}1,2}), \boldsymbol{f}_3^{\times}\boldsymbol{f}_2(\boldsymbol{q}_{i\text{–}1,2}) \end{bmatrix} \begin{bmatrix} {}^{B_{i-1}}_{P_i}\omega_{B_{ix}} \\ {}^{B_{i-1}}_{P_i}\omega_{B_{iy}} \end{bmatrix}. \tag{15} $$

Therefore, the linear free-mode matrix $\boldsymbol{\Phi}_{i\boldsymbol{v}} = [-l_{i\text{–}1}\boldsymbol{f}_3^{\times}\boldsymbol{f}_1(\boldsymbol{q}_{i\text{–}1,2}),\ -l_{i\text{–}1}\boldsymbol{f}_3^{\times}\boldsymbol{f}_2(\boldsymbol{q}_{i\text{–}1,2})]$ is obtained, which describes the generated linear motion of $\sum B_i$ relative to $\sum B_{i\text{–}1}$ when an SRC joint velocity is given.

Combining (11) and (15), the free-mode matrix $\boldsymbol{\Phi}_i$ of the SRC joint in (8) can be expressed as

$$ \boldsymbol{\Phi}_i = \begin{bmatrix} \boldsymbol{f}_1(\boldsymbol{q}_{i\text{–}1,2}) & \boldsymbol{f}_2(\boldsymbol{q}_{i\text{–}1,2}) \\ -l_{i\text{–}1}\boldsymbol{f}_3^{\times}\boldsymbol{f}_1(\boldsymbol{q}_{i\text{–}1,2}) & -l_{i\text{–}1}\boldsymbol{f}_3^{\times}\boldsymbol{f}_2(\boldsymbol{q}_{i\text{–}1,2}) \end{bmatrix} \tag{16} $$

which reflects the spatial velocity of the body $\sum B_i$ relative to the body $\sum B_{i\text{–}1}$ due to the SRC joint velocity.

TABLE I
JOINT MODEL FORMULAS FOR TWO-DOF SRC JOINT

Joint type	TWO-DOF SRC
Rotation matrix, ${}^{B_{i-1}}\boldsymbol{R}_{B_i}$	[see Eq.(6)]
Position vector, ${}^{B_{i-1}}_{P_i}\boldsymbol{r}_{B_i}$	$\begin{bmatrix} 0 \\ 0 \\ l_i + l_{i-1} \end{bmatrix}$
Free modes, $\boldsymbol{\Phi}_i$	$\begin{bmatrix} \boldsymbol{f}_1(\boldsymbol{q}_{i-1,2}) & \boldsymbol{f}_2(\boldsymbol{q}_{i-1,2}) \\ l_{i-1}\boldsymbol{f}_3^{\times}\boldsymbol{f}_1(\boldsymbol{q}_{i-1,2}) & l_{i-1}\boldsymbol{f}_3^{\times}\boldsymbol{f}_2(\boldsymbol{q}_{i-1,2}) \end{bmatrix}$
Pose variables	$\boldsymbol{q}_i$
Velocity variables	$\begin{bmatrix} {}^{B_{i-1}}_{P_i}\omega_{B_{ix}} \\ {}^{B_{i-1}}_{P_i}\omega_{B_{iy}} \end{bmatrix}$

As a summary, Section II establishes the SRC joint model, which describes the motion of frame $\sum B_i$ fixed in one body of the SRC joint relative to frame $\sum B_{i-1}$ fixed in the other body. The motion is expressed as a function of the SRC joint motion variables $\boldsymbol{q}_i$ and ${}^{B_{i-1}}_{P_i}\omega_{B_{ix}}$, ${}^{B_{i-1}}_{P_i}\omega_{B_{iy}}$, and other elements of the SRC joint. As with other classic robot joints (see [8, Tables 2.5 and 2.6]), the SRC joint's elements include the rotation matrix ${}^{B_{i-1}}\boldsymbol{R}_{B_i}$, position vector ${}^{B_{i-1}}_{P_i}\boldsymbol{r}_{B_i}$, and free modes $\boldsymbol{\Phi}_i$, which have been summarized and listed in Table I. The elements are also important for deriving the kinematics model of the robot manipulator composed of the SRC joints in Section III.

III. KINEMATICS MODELING OF THE SRC JOINT MANIPULATOR

In this section, a serial robot manipulator composed of SRC joints is presented, as shown in Fig. 2, with its forward kinematics and IK being thoroughly modeled.

Three kinds of coordinate frame are defined to describe relative motions among the manipulator bodies: inertial frame $\sum I$, link body-fixed frame $\sum B_i$, and virtual tangent plane body-fixed frame $\sum P_i$ (also as the joint frame), where $i = 1, \ldots, n$; n is the number of joints/links. B_0 represents the base of the manipulator; the last link B_n is treated as the end-effector. Define the position of the geometry center of the spherical link B_i in the inertial frame $\sum I$ as ${}^I_I\boldsymbol{r}_{B_i}$, the orientation of link B_i relative to $\sum I$ as the unit quaternion $\boldsymbol{q}_{i,I}$, and the radius of the link B_i as l_i.

A. Forward Kinematics

The *forward kinematics* of the serial SRC joint manipulator determines the pose (i.e., position and orientation) of the end-effector, ${}^I_I\boldsymbol{r}_{B_n}$ and $\boldsymbol{q}_{n,I}$ (or its linear and angular velocities, ${}^I_I\boldsymbol{v}_{B_n}$ and ${}^I_I\boldsymbol{\omega}_{B_n}$, in the *forward instantaneous kinematics* problem), given the positions $\boldsymbol{q}_i$ (or velocities ${}^{B_{i-1}}_{P_i}\omega_{B_{ix}}$ and ${}^{B_{i-1}}_{P_i}\omega_{B_{iy}}$) of all of the SRC joints and the values of all of the geometric link parameters l_i.

For the SRC joint manipulator, we have

$$ {}^I\boldsymbol{R}_{B_n} = {}^I\boldsymbol{R}_{B_0} \prod_{i=1}^{n} \left({}^{B_{i-1}}\boldsymbol{R}_{B_i} \right). \tag{17} $$

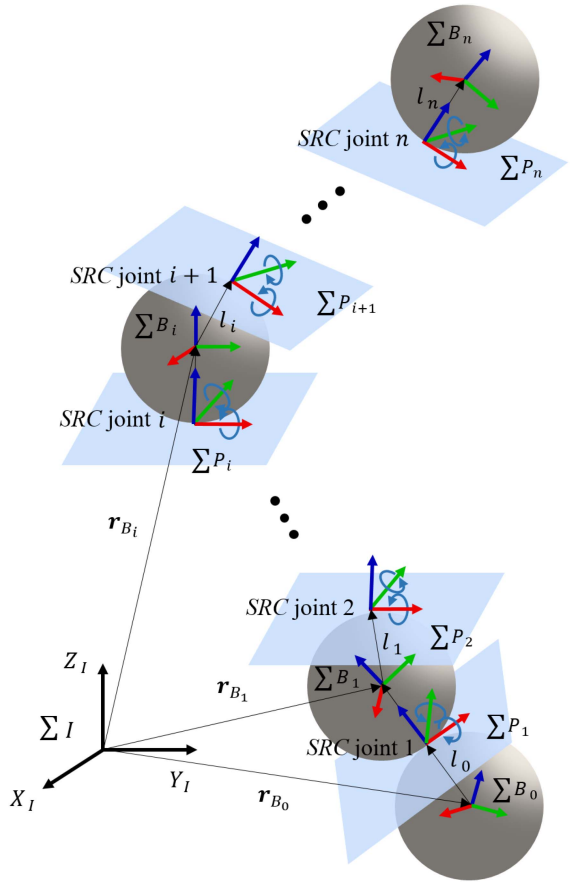

Fig. 2. Diagram of the serial SRC joint manipulator.

Given the SRC joint positions $\boldsymbol{q}_i$, the rotation matrices of the SRC joints ${}^{B_{i-1}}\boldsymbol{R}_{B_i}$ are calculated, as shown in Section II-A. Without loss of generality, ${}^{I}\boldsymbol{R}_{B_0}$ is the identity matrix when the base B_0 is fixed. Therefore, the rotation matrix of the end-effector with respect to the inertial frame, ${}^{I}\boldsymbol{R}_{B_n}$, can be calculated from $\boldsymbol{q}_i$. Then, the orientation of the end-effector relative to the inertial frame, $\boldsymbol{q}_{n,I}$, can be extracted from ${}^{I}\boldsymbol{R}_{B_n}$ [8].

In order to calculate the angular velocity of the end-effector in the inertial frame ${}^{I}_{I}\boldsymbol{\omega}_{B_n}$ when given the velocities ${}^{B_{i-1}}_{P_i}\omega_{B_{ix}}$ and ${}^{B_{i-1}}_{P_i}\omega_{B_{iy}}$ of all of the SRC joints, according to the free modes of the SRC joint $\boldsymbol{\Phi}_i$ in Table I, one first has

$$ {}^{B_{i-1}}_{B_{i-1}}\boldsymbol{\omega}_{B_i} = \boldsymbol{\Phi}_{i\boldsymbol{\omega}} \begin{bmatrix} {}^{B_{i-1}}_{P_i}\omega_{B_{ix}} \\ {}^{B_{i-1}}_{P_i}\omega_{B_{iy}} \end{bmatrix}. \tag{18} $$

Then, the angular velocity ${}^{I}_{I}\boldsymbol{\omega}_{B_i}, i = 1, \ldots, n$, can be iteratively calculated as (iterative process refers to Appendix B1)

$$ {}^{I}_{I}\boldsymbol{\omega}_{B_i} = \sum_{j=1}^{i} \left({}^{I}\boldsymbol{R}_{B_{j-1}} \boldsymbol{\Phi}_{j\boldsymbol{\omega}} \begin{bmatrix} {}^{B_{j-1}}_{P_j}\omega_{B_{jx}} \\ {}^{B_{j-1}}_{P_j}\omega_{B_{jy}} \end{bmatrix} \right) + {}^{I}_{I}\boldsymbol{\omega}_{B_0}. \tag{19} $$

Especially, one has

$$ {}^{I}_{I}\boldsymbol{\omega}_{B_n} = \sum_{i=1}^{n} \left({}^{I}\boldsymbol{R}_{B_{i-1}} \boldsymbol{\Phi}_{i\boldsymbol{\omega}} \begin{bmatrix} {}^{B_{i-1}}_{P_i}\omega_{B_{ix}} \\ {}^{B_{i-1}}_{P_i}\omega_{B_{iy}} \end{bmatrix} \right) + {}^{I}_{I}\boldsymbol{\omega}_{B_0}. \tag{20} $$

By defining the involved SRC joint velocity set

$$ \boldsymbol{\omega} = \begin{bmatrix} {}^{B_0}_{P_1}\omega_{B_{1x}} \\ {}^{B_0}_{P_1}\omega_{B_{1y}} \\ \vdots \\ {}^{B_{n-1}}_{P_n}\omega_{B_{nx}} \\ {}^{B_{n-1}}_{P_n}\omega_{B_{ny}} \end{bmatrix} \in \mathbb{R}^{2n} \tag{21} $$

as in (19) and (20), the *forward angular velocity equations* of the SRC joint manipulator can be obtained as follows:

$$ {}^{I}_{I}\boldsymbol{\omega}_{B_i} = {}^{I}_{I}\boldsymbol{\omega}_{B_0} + \boldsymbol{J}_{B_i\boldsymbol{\omega}}\,\boldsymbol{\omega} \tag{22} $$

$$ {}^{I}_{I}\boldsymbol{\omega}_{B_n} = {}^{I}_{I}\boldsymbol{\omega}_{B_0} + \boldsymbol{J}_{B_n\boldsymbol{\omega}}\,\boldsymbol{\omega} \tag{23} $$

where $\boldsymbol{J}_{B_i\boldsymbol{\omega}}$ and $\boldsymbol{J}_{B_n\boldsymbol{\omega}}$ are termed as the angular Jacobian matrices of the SRC joint manipulator that map the joint velocities into the angular velocities of the link i and end-effector, and

$$ \boldsymbol{J}_{B_i\boldsymbol{\omega}} = \begin{bmatrix} {}^{I}\boldsymbol{R}_{B_0}\boldsymbol{\Phi}_{1\boldsymbol{\omega}} & \cdots & {}^{I}\boldsymbol{R}_{B_{i-1}}\boldsymbol{\Phi}_{i\boldsymbol{\omega}} & \boldsymbol{0} & \cdots & \boldsymbol{0} \end{bmatrix} \in \mathbb{R}^{3\times 2n} \tag{24} $$

$$ \boldsymbol{J}_{B_n\boldsymbol{\omega}} = \begin{bmatrix} {}^{I}\boldsymbol{R}_{B_0}\boldsymbol{\Phi}_{1\boldsymbol{\omega}} & \cdots & {}^{I}\boldsymbol{R}_{B_{n-1}}\boldsymbol{\Phi}_{n\boldsymbol{\omega}} \end{bmatrix} \in \mathbb{R}^{3\times 2n}. \tag{25} $$

The positions ${}^{I}_{I}\boldsymbol{r}_{B_i}$ and ${}^{I}_{I}\boldsymbol{r}_{B_n}$ are calculated as follows:

$$ {}^{I}_{I}\boldsymbol{r}_{B_i} = {}^{I}_{I}\boldsymbol{r}_{B_0} + \sum_{j=1}^{i} \left({}^{I}\boldsymbol{R}_{B_{j-1}} {}^{B_{j-1}}_{B_{j-1}}\boldsymbol{r}_{B_j} \right) \tag{26} $$

$$ {}^{I}_{I}\boldsymbol{r}_{B_n} = {}^{I}_{I}\boldsymbol{r}_{B_0} + \sum_{i=1}^{n} \left({}^{I}\boldsymbol{R}_{B_{i-1}} {}^{B_{i-1}}_{B_{i-1}}\boldsymbol{r}_{B_i} \right). \tag{27} $$

According to the free modes of the SRC joint $\boldsymbol{\Phi}_i$ in Table I, one has

$$ {}^{B_{i-1}}_{B_{i-1}}\boldsymbol{v}_{B_i} = \boldsymbol{\Phi}_{i\boldsymbol{v}} \begin{bmatrix} {}^{B_{i-1}}_{P_i}\omega_{B_{ix}} \\ {}^{B_{i-1}}_{P_i}\omega_{B_{iy}} \end{bmatrix}. \tag{28} $$

Differentiating (26) and using the relations (22) and (28) results in (a more detailed derivation refers to Appendix B2)

$$ {}^{I}_{I}\boldsymbol{v}_{B_i} = {}^{I}_{I}\boldsymbol{v}_{B_0} + {}^{I}_{I}\boldsymbol{r}^{\times}_{0i}\,{}^{I}_{I}\boldsymbol{\omega}_{B_0} + \boldsymbol{J}_{B_i\boldsymbol{v}}\boldsymbol{\omega} \tag{29} $$

where $\boldsymbol{J}_{B_i\boldsymbol{v}}$ is termed as the linear Jacobian matrix of the SRC joint manipulator that maps the joint velocities into the linear velocity of the geometry center of the link i, and

$$ {}^{I}_{I}\boldsymbol{r}_{0i} = {}^{I}_{I}\boldsymbol{r}_{B_0} - {}^{I}_{I}\boldsymbol{r}_{B_i} = -\sum_{j=1}^{i} {}^{B_{j-1}}_{I}\boldsymbol{r}_{B_j} \in \mathbb{R}^3 \tag{30} $$

$$ \boldsymbol{J}'_{B_i\boldsymbol{v}} = \begin{bmatrix} {}^{I}\boldsymbol{R}_{B_0}\boldsymbol{\Phi}_{1\boldsymbol{v}} & \cdots & {}^{I}\boldsymbol{R}_{B_{i-1}}\boldsymbol{\Phi}_{i\boldsymbol{v}} & \boldsymbol{0} & \cdots & \boldsymbol{0} \end{bmatrix} \in \mathbb{R}^{3\times 2n} \tag{31} $$

$$ \boldsymbol{J}_{B_i\boldsymbol{v}} = \boldsymbol{J}'_{B_i\boldsymbol{v}} - \sum_{j=1}^{i} \left({}^{B_{j-1}}_{I}\boldsymbol{r}^{\times}_{B_j} \boldsymbol{J}_{B_{j-1}\boldsymbol{\omega}} \right) \in \mathbb{R}^{3\times 2n}. \tag{32} $$

Similarly, (27) can be derived and results in

$$ {}^{I}_{I}\boldsymbol{v}_{B_n} = {}^{I}_{I}\boldsymbol{v}_{B_0} + {}^{I}_{I}\boldsymbol{r}^{\times}_{0n}\,{}^{I}_{I}\boldsymbol{\omega}_{B_0} + \boldsymbol{J}_{B_n\boldsymbol{v}}\boldsymbol{\omega} \tag{33} $$

where $\boldsymbol{J}_{B_n\boldsymbol{v}}$ is the linear Jacobian matrix that maps the joint velocities into the linear velocity of the end-effector

$$ {}^{I}_{I}\boldsymbol{r}_{0n} = {}^{I}_{I}\boldsymbol{r}_{B_0} - {}^{I}_{I}\boldsymbol{r}_{B_n} = -\sum_{i=1}^{n} {}^{B_{i-1}}_{I}\boldsymbol{r}_{B_i} \in \mathbb{R}^3 \tag{34} $$

$$ \boldsymbol{J}'_{B_n\boldsymbol{v}} = \begin{bmatrix} {}^{I}\boldsymbol{R}_{B_0}\boldsymbol{\Phi}_{1\boldsymbol{v}} & \cdots & {}^{I}\boldsymbol{R}_{B_{n-1}}\boldsymbol{\Phi}_{n\boldsymbol{v}} \end{bmatrix} \in \mathbb{R}^{3\times 2n} \tag{35} $$

$$ \boldsymbol{J}_{B_n\boldsymbol{v}} = \boldsymbol{J}'_{B_n\boldsymbol{v}} - \sum_{i=1}^{n} \left({}^{B_{i-1}}_{I}\boldsymbol{r}^{\times}_{B_i}\boldsymbol{J}_{B_{i-1}\boldsymbol{\omega}} \right) \in \mathbb{R}^{3\times 2n}. \tag{36} $$

Equations (29) and (33) present the *forward linear velocity equations* of the SRC joint manipulator.

B. Inverse Kinematics

The IK problem for the SRC joint manipulator is to find the values of the SRC joint positions $\boldsymbol{q}_i$ (or velocities ${}^{B_{i-1}}_{P_i}\omega_{B_{ix}}$ and ${}^{B_{i-1}}_{P_i}\omega_{B_{iy}}$ in the *inverse instantaneous kinematics* problem) given the poses, ${}^{I}_{I}\boldsymbol{r}_{B_n}$ and $\boldsymbol{q}_{n,I}$ (or linear and angular velocities, ${}^{I}_{I}\boldsymbol{v}_{B_n}$ and ${}^{I}_{I}\boldsymbol{\omega}_{B_n}$) of the end-effector relative to the inertial frame and the values of all the geometric link parameters l_i.

Given the forward kinematics equations of the SRC joint manipulator, i.e., (17) and (27), it is clear that the IK problem for the SRC joint manipulator requires the solution of sets of nonlinear equations and is difficult to be presented in closed form. This section presents the damped least squares (DLS)-based IK method for the SRC joint manipulator, which first obtains the smooth SRC joint velocities that correspond to a desired end-effector velocity, i.e., the inverse instantaneous kinematics problem of the SRC joint manipulator is solved. Then, the SRC joint positions, which correspond to the specific pose of the end-effector, can be obtained by performing the joint velocity integration resulted from the velocities of the end-effector that lead to its desired pose and orientation.

In order to obtain the required SRC joint velocities $\boldsymbol{\omega}$ that guarantee the desired linear and angular velocities of the end-effector simultaneously, the *forward linear and angular velocity equations* (23) and (33) are combined together

$$ \begin{bmatrix} {}^{I}_{I}\boldsymbol{v}_{B_n} \\ {}^{I}_{I}\boldsymbol{\omega}_{B_n} \end{bmatrix} = \begin{bmatrix} \boldsymbol{I}_3 & {}^{I}_{I}\boldsymbol{r}^{\times}_{0n} \\ \boldsymbol{0} & \boldsymbol{I}_3 \end{bmatrix} \begin{bmatrix} {}^{I}_{I}\boldsymbol{v}_{B_0} \\ {}^{I}_{I}\boldsymbol{\omega}_{B_0} \end{bmatrix} + \begin{bmatrix} \boldsymbol{J}_{B_n\boldsymbol{v}} \\ \boldsymbol{J}_{B_n\boldsymbol{\omega}} \end{bmatrix} \boldsymbol{\omega} \tag{37} $$

where $\boldsymbol{I}_3$ is the identity matrix.

Without loss of generality, this article supposes that the SRC joint manipulator has a fixed base; (37) can be simplified as

$$ \begin{bmatrix} {}^{I}_{I}\boldsymbol{v}_{B_n} \\ {}^{I}_{I}\boldsymbol{\omega}_{B_n} \end{bmatrix} = \boldsymbol{J}_{B_n}\boldsymbol{\omega} \tag{38} $$

where $\boldsymbol{J}_{B_n} = [\boldsymbol{J}^{\top}_{B_n\boldsymbol{v}}, \boldsymbol{J}^{\top}_{B_n\boldsymbol{\omega}}]^{\top} \in \mathbb{R}^{6\times 2n}$ is termed as the Jacobian matrix of the SRC joint manipulator.

Using the adaptive DLS method to solve the kinematics equations (38), one performs singular value decomposition on the Jacobian matrix $\boldsymbol{J}_{B_n}$ [28]

$$ \boldsymbol{J}_{B_n} = \boldsymbol{U}\boldsymbol{\Sigma}\boldsymbol{V}^{\top} \tag{39} $$

where $\boldsymbol{U} \in \mathbb{R}^{6\times 6}$ and $\boldsymbol{V} \in \mathbb{R}^{2n\times 2n}$ are unitary matrices composed of the left- and right-singular vectors of $\boldsymbol{J}_{B_n}$. $\boldsymbol{\Sigma} \in \mathbb{R}^{6\times 2n}$ is a rectangular diagonal matrix with singular values of $\boldsymbol{J}_{B_n}$ on the diagonal, which is calculated as

$$ \boldsymbol{\Sigma} = \begin{bmatrix} \sigma_1 & \cdots & 0 & 0 & \cdots & 0 \\ \vdots & \ddots & \vdots & \vdots & & \vdots \\ 0 & \cdots & \sigma_6 & 0 & \cdots & 0 \end{bmatrix}, \quad \text{for } 6 \le 2n \tag{40} $$

and

$$ \boldsymbol{\Sigma} = \begin{bmatrix} \sigma_1 & \cdots & 0 \\ \vdots & \ddots & \vdots \\ 0 & \cdots & \sigma_{2n} \\ 0 & \cdots & 0 \\ \vdots & & \vdots \\ 0 & \cdots & 0 \end{bmatrix}, \quad \text{for } 6 > 2n \tag{41} $$

with σ_i being the singular values ordered so that $\sigma_1 \ge \cdots \ge \sigma_r > 0$ and $\sigma_{r+1} = \cdots = \sigma_{\min(6,2n)} = 0$; r is the rank of $\boldsymbol{J}_{B_n}$.

Using (39), the adaptive DLS-based IK solution of (38) is [29], [30]

$$ \boldsymbol{\omega} = \boldsymbol{V}\boldsymbol{\Sigma}^{*}\boldsymbol{U}^{\top} \begin{bmatrix} {}^{I}_{I}\boldsymbol{v}_{B_n} \\ {}^{I}_{I}\boldsymbol{\omega}_{B_n} \end{bmatrix} \tag{42} $$

where $\boldsymbol{\Sigma}^{*} \in \mathbb{R}^{2n\times 6}$ is the pseudoinverse of $\boldsymbol{\Sigma}$ and formed by replacing every nonzero diagonal entry σ_i of $\boldsymbol{\Sigma}$ with its damped reciprocal

$$ \sigma^{*}_i = \frac{\sigma_i}{\sigma_i^2 + \lambda^2}, \qquad i = 1, \ldots, r \tag{43} $$

and transposing the resulting matrix. The damping factor λ^2 is adaptively adopted according to the following law:

$$ \lambda^2 = \begin{cases} 0, & \text{if } \sigma_{\min(6,2n)} \ge \xi \\ \left(1 - \left(\frac{\sigma_r}{\xi}\right)^2\right)\lambda^2_{\max}, & \text{otherwise} \end{cases} \tag{44} $$

where σ_r is the smallest positive singular value of $\boldsymbol{J}_{B_n}$, and ξ defines the size of the singular region; the value of $\lambda_{\max}$ is at user's disposal to suitably shape the solution in the neighborhood of a singularity.

The smooth SRC joint velocity $\boldsymbol{\omega}$ that corresponds to the specific end-effector velocities ${}^{I}_{I}\boldsymbol{v}_{B_n}$ and ${}^{I}_{I}\boldsymbol{\omega}_{B_n}$ can be obtained using (42). In order to solve the joint positions $\boldsymbol{q}_i$ that corresponds to the desired pose of the end-effector, ${}^{I}_{I}\boldsymbol{r}_{B_n}$ and $\boldsymbol{q}_{n,I}$, a closed-loop reference velocity profile ${}^{I}_{I}\boldsymbol{v}^{r}_{B_n}$ and ${}^{I}_{I}\boldsymbol{\omega}^{r}_{B_n}$ for the end-effector reaching the desired pose is designed as follows:

$$ {}^{I}_{I}\boldsymbol{v}^{r}_{B_n} = {}^{I}_{I}\dot{\boldsymbol{r}}^{d}_{B_n} + \boldsymbol{K}_p({}^{I}_{I}\boldsymbol{r}^{d}_{B_n} - {}^{I}_{I}\boldsymbol{r}_{B_n}) \tag{45} $$

$$ {}^{I}_{I}\boldsymbol{\omega}^{r}_{B_n} = {}^{I}_{I}\boldsymbol{\omega}^{d}_{B_n} + \boldsymbol{K}_a\boldsymbol{\delta}_{B_n,\text{Quat}} \tag{46} $$

$$ \boldsymbol{\delta}_{B_n,\text{Quat}} = \eta_{n,I}\boldsymbol{\epsilon}^{d}_{n,I} - \eta^{d}_{n,I}\boldsymbol{\epsilon}_{n,I} - \boldsymbol{\epsilon}^{d}_{n,I} \times \boldsymbol{\epsilon}_{n,I} \tag{47} $$

where the right superscript "d" denotes the desired values, $\eta_{n,I}$ and $\boldsymbol{\epsilon}_{n,I}$ are the scalar and vector parts of $\boldsymbol{q}_{n,I}$, respectively, and the resulting end-effector orientation errors can be calculated using (47). $\boldsymbol{K}_p, \boldsymbol{K}_a \in \mathbb{R}^{3\times 3}$ are suitable positive-definite matrix gains. It is readily to prove that the end-effector pose errors

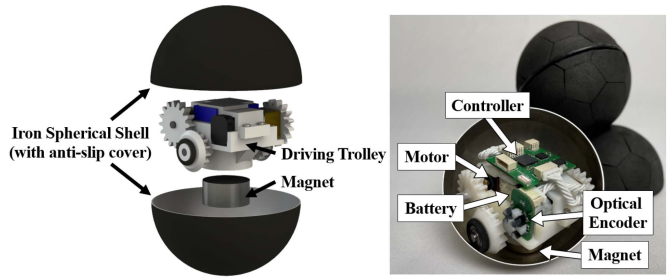

Fig. 3. Components of a FreeBOT module.

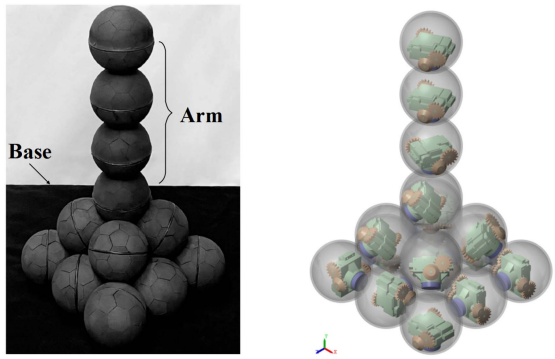

Fig. 4. FreeBOT realization of the SRC joint manipulator.

globally asymptotically converge to zeros by following the velocity profile ${}^{I}_{I}\boldsymbol{v}^{r}_{B_n}$ and ${}^{I}_{I}\boldsymbol{\omega}^{r}_{B_n}$ [31]. Given the end-effector reference velocities ${}^{I}_{I}\boldsymbol{v}^{r}_{B_n}$ and ${}^{I}_{I}\boldsymbol{\omega}^{r}_{B_n}$, the corresponding SRC joint reference velocities $\boldsymbol{\omega}^{r}$ are solved using (42). Then, the required joint positions $\boldsymbol{q}^{r}_{i}$ for reaching the desired end-effector pose are obtained by performing the joint reference velocity integration using the SRC joint model in Section II.

C. Discussion

The SRC joint manipulator has the advantages of the enlargement of motion range, the absence of abrasion wear, provision of a transmission ratio directly at the joint, etc. It is worth noting that due to the geometric symmetry of the spherical units, the SRC joints can roll forward flexibly in all directions, such that the manipulator can easily perform tasks in environments with static and dynamic obstacles, as well as in narrow spaces. The drive of the SRC joint can also be novelly physically implemented. Unlike conventional robotic manipulator that use combinations of revolute and prismatic joints implemented by dc motors, the realization of the SRC joint could be using the FreeBOT for example [27], as shown in detail in Section IV, where a driving trolley moves inside the spherical iron body and uses a magnet at trolley's bottom to attract the other body not separated. In turn, performing chain-type motion is common for a modular self-reconfigurable robot (MSRR) robot (like FreeBOT) in self-reconfiguration tasks [32], the established SRC joint model and manipulator kinematics are also useful for describing the reconfiguration motions of the FreeBOT.

IV. Control of the SRC Joint Manipulator

An MSRR robot whose module can be freely connected, termed as FreeBOT, has been proposed by Liang et al. [27]. This section uses FreeBOTs to realize the kinematic motion of the two-DOF SRC joint and manipulator composed of SRC joints. The desired SRC joint motions are translated into those of the driving trolley inside the FreeBOT through path planning; then, the control method is proposed for the trolley, such that the trolley drives the SRC joint and end-effector of the manipulator to move as expected.

A. FreeBOT Components

As shown in Fig. 3, a FreeBOT is mainly composed of an iron sphere shell, a differential-wheel-driven trolley inside the shell, a permanent magnet at the trolley bottom, and other measurement and control units. When a FreeBOT moves over another one, the magnetic force between the permanent magnet of one FreeBOT and the iron shell of the other FreeBOT guarantees the two FreeBOTs not separated. A layer of ethylene-vinyl acetate (EVA) foam is applied to the outer surface of the iron sphere shell to increase friction forces and torques, such that the two FreeBOTs roll relatively without slipping at the contact point, and the rotation about the vertical axis of the tangent plane at the contact point is avoided.

Obviously, the two-DOF SRC joint is singularity-free when the driving trolley is holonomic, for instance, using omnidirectional wheels. Differential-wheel driven trolley, on the other hand, is widely used in robotics owing to its simplicity. In a FreeBOT, the trolley *steers* freely inside the shell about the vertical axis of the tangent plane and *moves forward* along an arbitrary direction inside the tangent plane; thus, the two-DOF motions of the SRC joint are realized. The relationships between the trolley steering and forward velocities and the SRC joint velocities ${}^{B_{i-1}}_{P_i}\boldsymbol{\omega}_{B_i}$ are discussed in Section IV-B.

In this article, a Lyapunov-based control method is proposed for the nonholonomic differential-wheel-driven trolley to realize the required motions of the SRC joint and manipulator. By taking the *first steering* to the desired angle, *then moving forward* strategy can also simulate the control effect of a holonomic trolley, i.e., simultaneously generating accurate two-DOF angular velocity of the SRC joint, which will be explained in detail in Section IV-C.

B. Trolley Path Planning

A serial-chain SRC joint manipulator formed by FreeBOTs is presented in Fig. 4. For the end-effector (assumed as the shell of the end FreeBOT) moving with specific velocities or reaching a desired pose, the corresponding SRC joint reference velocities $\boldsymbol{\omega}^{r}$ or final joint positions $\boldsymbol{q}^{r}_{i}$ have been obtained through solving the IK problem in Section III-B. This section determines the desired motions of the driving trolleys, such that the corresponding SRC joint can have the required velocity ${}^{B_{i-1}}_{P_i}\omega^{r}_{B_{ix}}, {}^{B_{i-1}}_{P_i}\omega^{r}_{B_{iy}}$ or reach the required joint position $\boldsymbol{q}^{r}_{i}$.

1) Velocity Planning: For the SRC joint generating the required angular velocity ${}^{B_{i-1}}_{P_i}\omega^{r}_{B_{ix}}, {}^{B_{i-1}}_{P_i}\omega^{r}_{B_{iy}}$, we define the *forward* and *steering* speeds of the driving trolley i as u_{if} and u_{is},

respectively, and denote the angular displacement of the trolley i caused by the steering motion as φ_i; the linear velocity of the trolley i in the tangent plane $\sum P_i$, i.e., ${}^{P_i}_{P_i}\boldsymbol{v}_{T_i}$, can be calculated as follows:

$$ {}^{P_i}_{P_i}\boldsymbol{v}_{T_i} = \begin{bmatrix} u_{if}\cos\varphi_i \\ u_{if}\sin\varphi_i \\ 0 \end{bmatrix} \tag{48} $$

with the steering dynamics

$$ \dot{\varphi}_i = u_{is} \tag{49} $$

where $\varphi_i = 0$ corresponds to that the forward direction of the trolley i points toward the $\hat{x}$-axis of $\sum P_i$.

According to the nonholonomic constraint that *rolling without slipping* occurs at the contact point between the two FreeBOTs, the following relationship exists:

$$ \begin{cases} {}^{P_i}_{P_i}v_{T_{ix}} - l_i {}^{P_i}_{P_i}\omega_{B_{iy}} = 0 \\ {}^{P_i}_{P_i}v_{T_{iy}} + l_i {}^{P_i}_{P_i}\omega_{B_{ix}} = 0 \end{cases}. \tag{50} $$

Substituting (48) and the SRC joint velocity relationship (1) into (50) results in

$$ \begin{cases} u_{if}\cos\varphi_i - l'_i {}^{B_{i-1}}_{P_i}\omega_{B_{iy}} = 0 \\ u_{if}\sin\varphi_i + l'_i {}^{B_{i-1}}_{P_i}\omega_{B_{ix}} = 0 \end{cases} \tag{51} $$

where $l'_i = l_i\, l_{i-1}/(l_i + l_{i-1})$.

Using (51), in order to generate the required SRC joint velocity ${}^{B_{i-1}}_{P_i}\omega^r_{B_{ix}}, {}^{B_{i-1}}_{P_i}\omega^r_{B_{iy}}$, the driving trolley i should move with the forward speed u^r_{if} along the specific direction φ^r_i, and u^r_{if} and φ^r_i are calculated as

$$ \begin{cases} u^r_{if} = l'_i\sqrt{\left({}^{B_{i-1}}_{P_i}\omega^r_{B_{ix}}\right)^2 + \left({}^{B_{i-1}}_{P_i}\omega^r_{B_{iy}}\right)^2} \\ \varphi^r_i = \text{atan2}\left(-{}^{B_{i-1}}_{P_i}\omega^r_{B_{ix}}/{}^{B_{i-1}}_{P_i}\omega^r_{B_{iy}}\right) \end{cases}. \tag{52} $$

2) Position Planning: For the SRC joint reaching the required joint position $\boldsymbol{q}^r_i$, the corresponding orientation of $\sum P_i$ relative to $\sum B_{i-1}$, represented by the unit quaternion $\widetilde{\boldsymbol{q}}^r_{i-1,2}$, is determined from $\boldsymbol{q}^r_i$ using the SRC joint model in Section II. The rotation matrix ${}^{B_{i-1}}\boldsymbol{R}^r_{P_i}$ is calculated from $\widetilde{\boldsymbol{q}}^r_{i-1,2}$. Therefore, the position of the contact point between the two FreeBOTs in $\sum B_{i-1}$, which corresponds to the required SRC joint position $\boldsymbol{q}^r_i$, is determined

$$ \begin{aligned} {}^{B_{i-1}}_{B_{i-1}}\boldsymbol{r}^r_{P_i} &= {}^{B_{i-1}}\boldsymbol{R}^r_{P_i}\, {}^{B_{i-1}}_{P_i}\boldsymbol{r}_{P_i} \\ &= {}^{B_{i-1}}\boldsymbol{R}^r_{P_i}\,[0,0,l_{i-1}]^\top \end{aligned} \tag{53} $$

which is constant and can be translated into the moving frame $\sum P_i$ as

$$ {}^{P_i}_{P_i}\boldsymbol{r}^r_{P_i} = {}^{P_i}\boldsymbol{R}_{B_{i-1}}({}^{B_{i-1}}_{B_{i-1}}\boldsymbol{r}^r_{P_i} - {}^{B_{i-1}}_{B_{i-1}}\boldsymbol{r}_{P_i}). \tag{54} $$

It is intuitive that the target position of the contact point, ${}^{P_i}_{P_i}\boldsymbol{r}^r_{P_i}$, can be expressed as going through a circular arc from its current position ${}^{P_i}_{P_i}\boldsymbol{r}_{P_i}$ in $\sum P_i$, given that the contact point always moves on the sphere surface of the FreeBOT B_{i-1}. There are two parameters to describe the reference circular arc, i.e., the arc distance s^r_i and the arc azimuth φ^r_i, which are calculated as

$$ \begin{cases} s^r_i = l_{i-1}\,\text{acos}\left(\left(l_{i-1} - \text{abs}\left({}^{P_i}_{P_i}\boldsymbol{r}^r_{P_iz}\right)\right)/l_{i-1}\right) \\ \varphi^r_i = \text{atan2}\left({}^{P_i}_{P_i}\boldsymbol{r}^r_{P_ix}/{}^{P_i}_{P_i}\boldsymbol{r}^r_{P_iy}\right) \end{cases}. \tag{55} $$

Therefore, in order to reach the required SRC joint position $\boldsymbol{q}^r_i$, the driving trolley i should go through the arc distance s^r_i along the specific direction φ^r_i in the tangent plane.

C. Trolley Control Method

Herein, the forward and steering speeds of the driving trolley u_{if} and u_{is}, as well as the rotation speeds of the two differential wheels w_{ir} and w_{il}, are sought, such that the driving trolley can move forward with the reference speed u^r_{if} or move through the reference arc distance s^r_i along the reference direction φ^r_i. As a result, the SRC joint (and correspondingly the end-effector) can have the reference velocities or reach the desired poses, respectively.

1) Forward and Steering Dependent: Following the steering dynamics of the trolley i in (49), the following trolley steering speed guarantees that the steering angle converges to the reference direction φ^r_i:

$$ u^r_{is} = \dot{\varphi}^r_i + k_{\varphi_{i,1}}(\varphi^r_i - \varphi_i). \tag{56} $$

In order to make the trolley i move forward with the speed u^r_{if} along the reference direction φ^r_i, which generates the reference SRC joint velocity ${}^{B_{i-1}}_{P_i}\omega^r_{B_{ix}}$ and ${}^{B_{i-1}}_{P_i}\omega^r_{B_{iy}}$ [as shown in (52)], it is designed that the trolley moves forward and steers simultaneously along the velocity

$$ \begin{cases} u_{if} = u^r_{if}\cos\varphi_{ie} \\ u_{is} = u^r_{is} + k_{\varphi_{i,2}}u^r_{if}\sin\varphi_{ie} \end{cases} \tag{57} $$

where φ_{ie} is the steering angle error, and $k_{\varphi_{i,1}}$ and $k_{\varphi_{i,2}}$ are positive constant gains.

Using (57) as the control rule of the trolley i, $\varphi_{ie} = 0$ is a uniformly asymptotically stable point. In this case, from (57), it is guaranteed that $u_{if} = u^r_{if}$, which means the trolley i can move forward with the speed u^r_{if} along the reference direction φ^r_i. As a result, the SRC joints (and correspondingly the end-effector) can have the reference velocities.

Proof: A scalar function V as a Lyapunov function candidate is proposed

$$ V = 1 - \cos\varphi_{ie}. \tag{58} $$

Clearly, $V \geq 0$. If $\varphi_{ie} = 0$, $V = 0$. If $\varphi_{ie} \neq 0$, $V > 0$.

Substituting the control rule (57) into the steering dynamics (49), one obtains the closed-loop steering dynamics

$$ \dot{\varphi}_{ie} = -k_{\varphi_{i,2}}u^r_{if}\sin\varphi_{ie}. \tag{59} $$

Therefore, one has

$$ \begin{aligned} \dot{V} &= \dot{\varphi}_{ie}\sin\varphi_{ie} \\ &= -k_{\varphi_{i,2}}u^r_{if}\sin^2\varphi_{ie} \leq 0. \end{aligned} \tag{60} $$

Then, V becomes a Lyapunov function.

By linearizing the differential equation (59) around $\varphi_{ie} = 0$, we obtain

$$\dot{\varphi}_{ie} + k_{\varphi_{i,2}} u_{if}^r \varphi_{ie} = 0. \tag{61}$$

It is readily to see that $k_{\varphi_{i,2}} u_{if}^r$ is continuously differentiable and is bounded. The characteristic equation for (61) is

$$s + k_{\varphi_{i,2}} u_{if}^r = 0. \tag{62}$$

From (52), there exists a positive constant δ such that $u_{if}^r \geq \delta$ for all $t \geq 0$. Therefore, the roots of (62) have real parts less than or equal to $-k_{\varphi_{i,2}}\delta$, which implies that $\varphi_{ie} = 0$ is a uniformly asymptotically stable point of (61). □

2) Forward and Steering Independent: In order to simulate the control effect of a holonomic driving trolley, i.e., simultaneously generating the accurate two-DOF SRC joint velocity, we adopt the *first steering* to the desired angle and *then moving forward* strategy. Although it requires extra time to wait for the convergence of the steering angle error φ_{ie}, the strategy is sufficient for performing the position movements in (55), such that the SRC joint can reach the required position $\boldsymbol{q}_i^r$.

Since the trolley is only required to steer first, one has $u_{if}^r = 0$. Therefore, the control rule of the trolley (57) is simplified as $u_{is} = u_{is}^r$ in (56), which guarantees that the steering angle converges to the reference direction φ_i^r.

Then, we design that the trolley moves forward with the speed

$$u_{if} = \dot{s}_i^r + k_{s_i}(s_i^r - s_i) \tag{63}$$

where k_{s_i} are positive constant gains.

Given the forward dynamics of the trolley i that $\dot{s}_i = u_{if}$, it is readily to prove that the forward speed in (63) guarantees the trolley going through the required arc distance s_i^r. Therefore, the SRC joint i reaches the required position $\boldsymbol{q}_i^r$. As a result, the end-effector reaches the desired pose ${}_I^I\boldsymbol{r}_{B_n}^d$ and $\boldsymbol{q}_{n,I}^d$ in the task space.

3) Wheel Speeds: For the FreeBOT shown in Fig. 3, the forward and steering speeds of the driving trolley and the rotation speeds of its two differential wheels satisfy the following relationships (refer to Appendix C):

$$\begin{cases} u_{if} = \frac{r_{i,\text{out}}\, r_{i,w}}{\sqrt{4\, r_{i,\text{in}}^2 - l_{i,w}^2}} \left(\omega_{ir} + \omega_{il}\right) \\ u_{is} = \frac{r_{i,w}}{l_{i,w}} \left(\omega_{ir} - \omega_{il}\right) \end{cases} \tag{64}$$

where w_{ir} and w_{il} represent the rotation speeds of the right and left wheels of the trolley i, respectively. Other parameters are defined in Fig. 5.

Having obtained the trolley forward and steering speeds u_{if} and u_{is} in the trolley control method, the wheel speeds that generate u_{if} and u_{is} can be solved from (64)

$$\begin{cases} w_{ir} = \frac{\sqrt{4\, r_{i,\text{in}}^2 - l_{i,w}^2}}{2\, r_{i,\text{out}}\, r_{i,w}} u_{if} + \frac{l_{i,w}}{2\, r_{i,w}} u_{is} \\ w_{il} = \frac{\sqrt{4\, r_{i,\text{in}}^2 - l_{i,w}^2}}{2\, r_{i,\text{out}}\, r_{i,w}} u_{if} - \frac{l_{i,w}}{2\, r_{i,w}} u_{is} \end{cases}. \tag{65}$$

Therefore, by applying rotation speeds in (65) to the differential wheels, the SRC joint and end-effector can realize the reference velocities, as well as the SRC joint can reach the reference joint position and the end-effector reaches the desired pose. A whole flowchart that brings the end-effector using FreeBOTs is presented in Fig. 6.

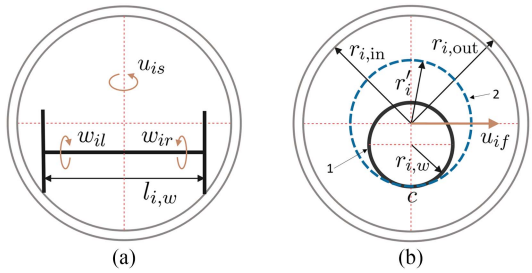

Fig. 5. Geometry parameters of the FreeBOT, $l_{i,w}$ is the wheel interval of the trolley, $r_{i,w}$ is the wheel radius of the trolley, and $r_{i,\text{out}}$ and $r_{i,\text{in}}$ are the outer and inner radii of the shell of the FreeBOT, respectively. (a) Rear view. (b) Right view.

V. Experiments

This article constructs a physics simulation system for the SRC joint and manipulator composed of FreeBOTs using the *Simscape Multibody* environment [33], termed as FreeBOT-SIM. The gravity, collision detection, and frictions, as well as the effects of magnetic forces among the FreeBOTs, can be successfully simulated. The wheel speeds of the driving trolley solved in Section IV-C are applied to the wheel block in FreeBOT-SIM, which causes the motions of the FreeBOT-SIM according to the physical laws. The FreeBOT-SIM provides a wide variety of sensors to measure the states of FreeBOTs, the SRC joint and manipulator. As a result, the SRC joint model, the kinematics models, and the path planning and control method of FreeBOTs can be readily validated using the FreeBOT-SIM.

A physical SRC joint manipulator is also built using real FreeBOTs, on which the effectiveness of the manipulator kinematics models and the path planning and control method of FreeBOTs are validated, by realizing that the manipulator moves as expected.

A. SRC *Joint Model Validation*

This section first validates the established two-DOF SRC joint model. Considering that the sizes of the two bodies connected by the SRC joint is generally different, as shown in Fig. 7, we form the two-DOF SRC joint in FreeBOT-SIM instead of using two real FreeBOTs that have the same size. The radii of the bodies B_i and B_{i-1} are 0.03 and 0.04 m, respectively. Assigning the angular velocity ${}_{P_i}^{P_i}\omega_{B_{ix}} = -0.1$ rad/s and ${}_{P_i}^{P_i}\omega_{B_{iy}} = -0.05$ rad/s at the SRC joint i, the motion sequences of the SRC joint at different time instants are presented in Fig. 7.

In order to validate the relationship between the SRC joint velocity ${}_{P_i}^{B_{i-1}}\boldsymbol{\omega}_{B_i}$ and ${}_{P_i}^{P_i}\omega_{B_{ix}}, {}_{P_i}^{P_i}\omega_{B_{iy}}$ in (1), the calculated SRC joint velocity using (1) and that measured using the FreeBOT-SIM sensor are presented in Fig. 8. The value consistency implies the correctness of the relationship in (1). The rotation matrix of the SRC joint i at different time instants when given ${}_{P_i}^{P_i}\omega_{B_{ix}}$ and ${}_{P_i}^{P_i}\omega_{B_{iy}}$ is calculated using the model equations in Section II, which represents the orientation of the body B_i relative to the body B_{i-1}. The orientation errors between the

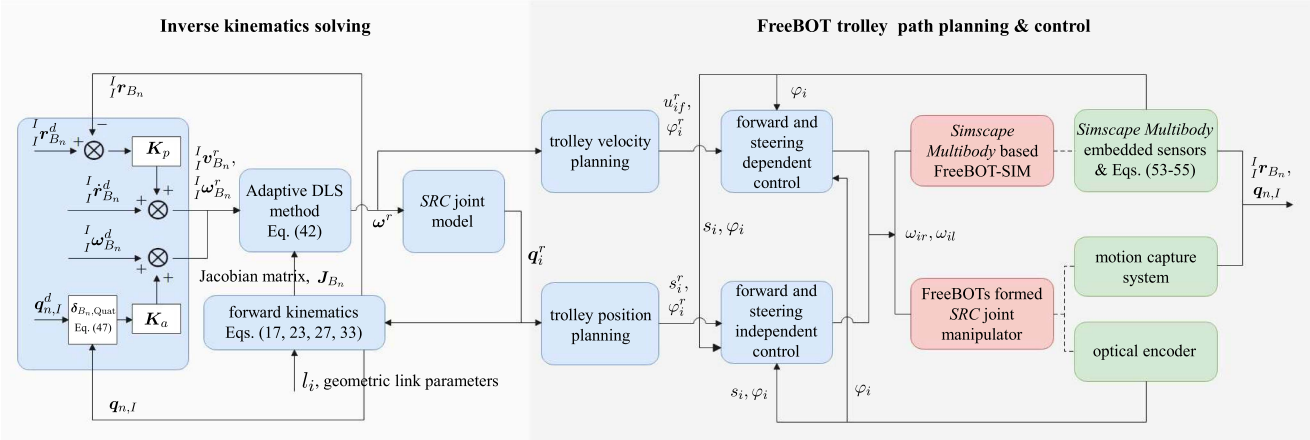

Fig. 6. Control diagram of the SRC joint manipulator using FreeBOTs.

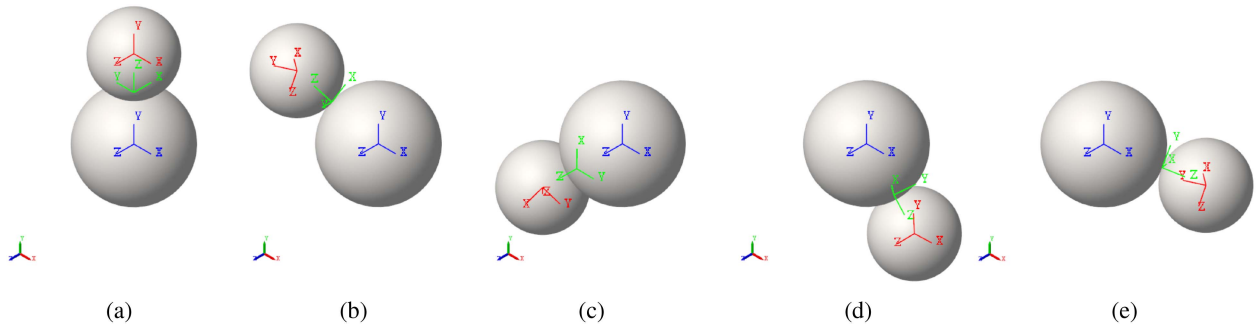

Fig. 7. Two-DOF SRC joint motion frames in FreeBOT-SIM with different body sizes. (a) $t = 0$ s. (b) $t = 5.9$ s. (c) $t = 14.9$ s. (d) $t = 24.2$ s. (e) $t = 30$ s.

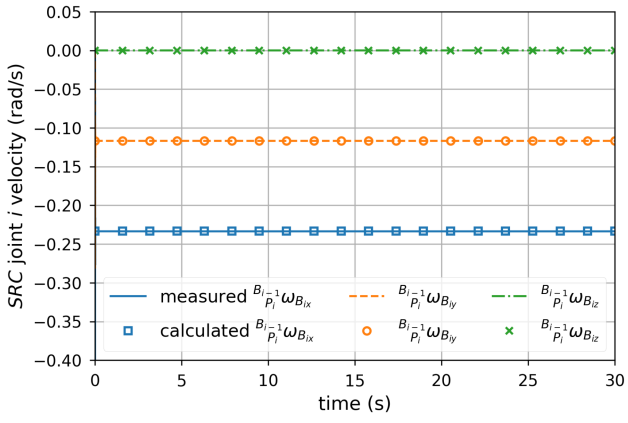

Fig. 8. Two-DOF SRC joint velocity measured and calculated using (1).

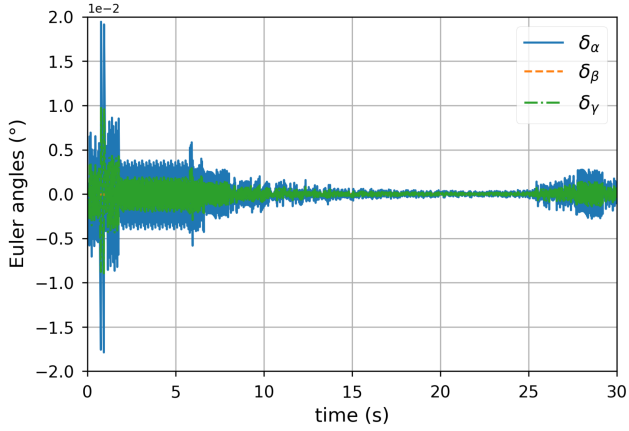

Fig. 9. Euler angles of the rotation matrix error of the SRC joint.

calculated values and that measured using the FreeBOT-SIM sensor are presented in Fig. 9, for intuitive purposes, which is represented using XYZ Euler angles. It can be seen that the peak angle error is smaller than $2\times10^{-2^\circ}$, and the average angle error is $[4.92, 0.01, 9.83] \times 10^{-4^\circ}$, which is mainly caused by the numerical integration errors. Therefore, the correctness of the rotation matrix model of the SRC joint is validated.

When applying the SRC joint velocity, the generated spatial velocity of the body B_i relative to B_{i-1}, i.e., ${}^{B_{i-1}}_{B_{i-1}}\boldsymbol{\nu}_{B_i}$, are calculated through the free-mode matrix $\boldsymbol{\Phi}_i$ in (8). The calculated spatial velocity ${}^{B_{i-1}}_{B_{i-1}}\boldsymbol{\nu}_{B_i}$ and that measured using the FreeBOT-SIM sensor are presented in Fig. 10. The coincidence of the calculated and measured values validates the correctness of the free-mode model of the SRC joint.

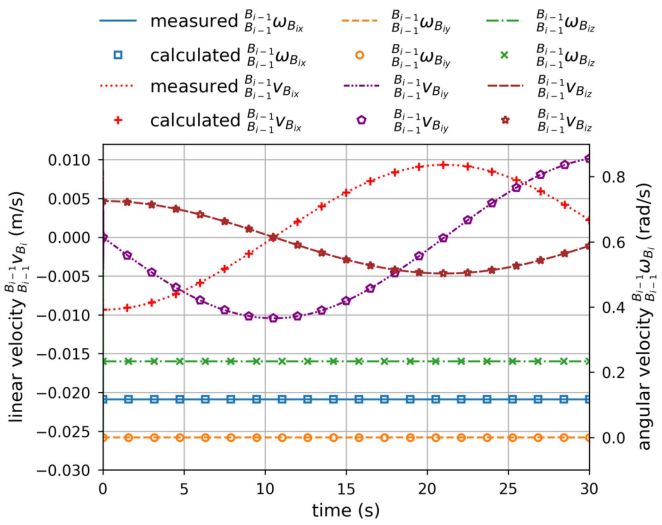

Fig. 10. Spatial velocity of B_i relative to B_{i-1} measured and calculated using the free-mode model.

TABLE II
KINEMATIC GEOMETRY AND CONTROL PARAMETERS OF THE SRC JOINT MANIPULATOR

Parameters	Values
$r_{i,\text{in}}$, $r_{i,\text{out}}$, l_i	0.032, 0.034, 0.034 m
$r_{i,w}$, $l_{i,w}$	0.005, 0.046 m
ξ, $\lambda_{\max}$	0.01
$\boldsymbol{K}_p$, $\boldsymbol{K}_a$	$2\boldsymbol{I}_n$
k_{s_i}, $k_{\varphi_{i,1}}$, $k_{\varphi_{i,2}}$	3, 6, 1
${}^I_I\boldsymbol{r}_{B_0}$	$[0\ \ 0\ \ 0]^\top$ m
$\boldsymbol{q}_{B_0,I}$	$[1\ \ 0\ \ 0\ \ 0]^\top$
$\boldsymbol{q}_1$, $\boldsymbol{q}_2$, $\boldsymbol{q}_3$, $\boldsymbol{q}_4$ at t_0	$[1\ \ 0\ \ 0\ \ 0]^\top$
$\boldsymbol{\varphi}(t_0)$	$[0.33\ \ 0.42\ \ 0.30\ \ 0.52]^\top$ rad
target ${}^I_I\boldsymbol{r}_A$	$[0.0036\ \ 0.1636\ \ 0.0924]^\top$ m
target ${}^I_I\boldsymbol{r}_B$	$[0.1151\ \ 0.1489\ \ 0.0291]^\top$ m
target ${}^I_I\boldsymbol{r}_C$	$[0.0924\ \ 0.1597\ \ 0.1154]^\top$ m
target $\boldsymbol{q}_{A,I}$	$[0.8610\ \ 0.4687\ \ 0.1356\ \ 0.1437]^\top$
target $\boldsymbol{q}_{B,I}$	$[0.8520\ \ 0.3289\ \ 0.2300\ \ 0.3362]^\top$
target $\boldsymbol{q}_{C,I}$	$[0.9682\ \ 0.0874\ \ 0.2220\ \ 0.0756]^\top$
obstacle 1, position	$[0.0948\ \ 0.0985\ \ 0.0467]^\top$ m
obstacle 2, position	$[0.0948\ \ 0.2107\ \ 0.0467]^\top$ m

B. SRC *Joint Manipulator Reaching Target Pose*

As shown in Fig. 4, a six-DOF SRC joint manipulator is built using FreeBOTs, and its simulation counterpart is constructed in the FreeBOT-SIM. In tasks where the end-effector of the SRC joint manipulator needs to reach a target pose, the required SRC joint positions are first solved using the proposed IK method in Section III-B and then realized with the FreeBOT driving trolley motions using the proposed path planning and control method. The kinematic geometry and control parameters of the SRC joint manipulator are listed in Table II.

Supposing that the end-effector needs to reach the target poses *A* and *B*, as shown in Table II, respectively, the corresponding SRC joint reference positions $\boldsymbol{q}_i^r$ are solved using the IK method

$$\begin{cases} \boldsymbol{q}_{1,A}^r = \begin{bmatrix} 0.7992 & 0.1912 & -0.5698 & 0.0016 \end{bmatrix} \\ \boldsymbol{q}_{2,A}^r = \begin{bmatrix} -0.5579 & -0.1939 & -0.7714 & -0.2366 \end{bmatrix} \\ \boldsymbol{q}_{3,A}^r = \begin{bmatrix} 0.1270 & -0.4998 & -0.3887 & 0.7636 \end{bmatrix} \end{cases} \tag{66}$$

and

$$\begin{cases} \boldsymbol{q}_{1,B}^r = \begin{bmatrix} -0.4558 & 0.5135 & -0.7261 & -0.0367 \end{bmatrix} \\ \boldsymbol{q}_{2,B}^r = \begin{bmatrix} -0.0130 & -0.6933 & 0.0267 & -0.7200 \end{bmatrix} \\ \boldsymbol{q}_{3,B}^r = \begin{bmatrix} 0.0880 & 0.2577 & 0.8231 & -0.4983 \end{bmatrix} \end{cases} . \tag{67}$$

Given the reference positions of the SRC joints, the trolley position planning (in Section IV-B2) and the *forward- and steering-independent* control (in Section IV-C2) strategies are adopted to drive the SRC joints to the reference joint positions. The required measurements of the real-time trolley direction φ_i and arc distance s_i are measured with simulated sensors and calculated using (53)–(55) in the FreeBOT-SIM and converted from the counts of the optical encoder mounted on the wheels in the physical manipulator. The pose of the end-effector is measured using the related FreeBOT-SIM sensors and motion capture system in the FreeBOT-SIM and physical system, respectively. Some motion frames captured at different time instants during the SRC joint manipulator reaching the target poses A and B are presented in Figs. 11 and 12, respectively. It can be seen that the simulated and physical manipulators go through the similar trajectories.

In order to show the motion precision of the SRC joint manipulator under the proposed method, the position and orientation errors of the end-effector during reaching the target poses A and B are presented in Figs. 13 and 14, respectively. It can be seen that the position and orientation errors of the end-effector finally converge to zero in both cases in the FreeBOT-SIM, which validates the effectiveness of the kinematics modeling of the SRC joint manipulator and the path planning and control methods of FreeBOTs. The final end-effector position errors are $[4.17, -0.21, -4.19]$ mm and $[-3.51, 3.9, 1.47]$ mm, and orientation errors (represented with XYZ Euler angles) are $[1.07, -0.8, 1.45]^\circ$ and $[0.13, 1.86, 0.52]^\circ$ for the physical manipulator reaching the target poses A and B, respectively. The experimental error is mainly caused by the deformation of the antislip EVA foam layer, which makes the spherical shell radius not exactly the same in the experiment and simulation. A slight slip may also happen due to the deformation of the EVA foam layer along the gravity direction.

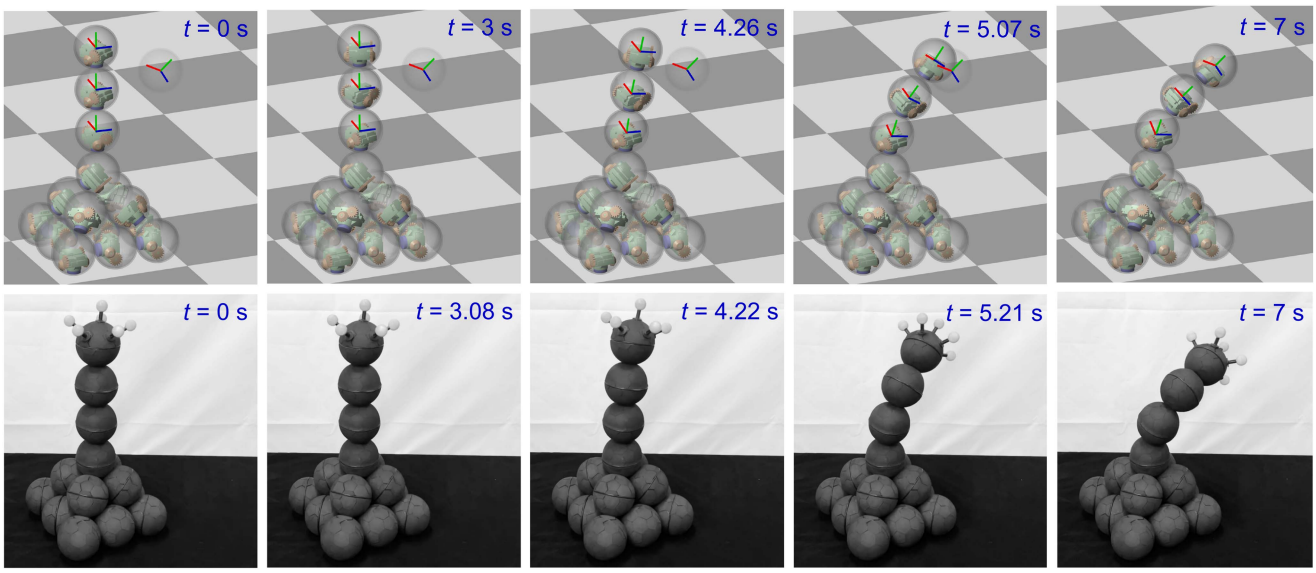

Fig. 11. Motion frames of the six-DOF SRC joint manipulator reaching the target pose *A*.

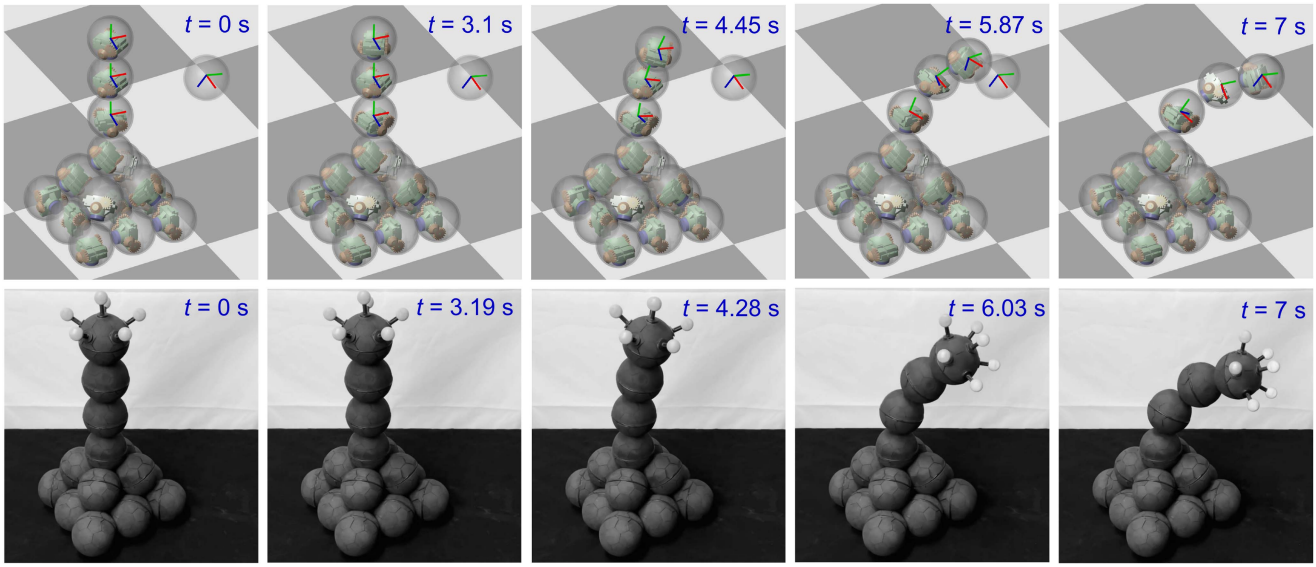

Fig. 12. Motion frames of the six-DOF SRC joint manipulator reaching the target pose *B*.

C. SRC *Joint Manipulator Avoiding Obstacles*

In a cluttered environment with obstacles, the SRC joint manipulator needs to complete specific tasks while avoiding obstacles. The SRC joint manipulator has the advantage of performing tasks in environments with obstacles or narrow space due to its geometric symmetry of spherical units. As shown in Fig. 15, the SRC joint manipulator needs to reach for the target pose C through the narrow space between the horizontal bars. Herein, the manipulator adopts the velocity damping method [34] to formulate the obstacle avoidance constraints using the established velocity kinematic equations (29). A sequence of quadratic programs that generalize the task-priority framework [35] are solved for the reference joint velocity, which formulate reaching the target pose and avoiding obstacles as equality and inequality constraints on joint velocity, respectively. Once the reference SRC joint velocity is obtained, the trolley velocity planning (in Section IV-B1) and the *forward- and steering-dependent* control (in Section IV-C1) strategy are used to ensure that the SRC joint moves along the reference velocity, so that the manipulator can avoid obstacles and the end-effector can reach the target pose.

The task-related parameters are listed in Table II. As shown in Fig. 15, the SRC joint manipulator smoothly avoids the obstacles in the narrow space and makes the end-effector successfully reach the target pose. It is worth pointing out that the SRC joint can easily roll toward the generated obstacle avoidance direction and determine the closest point on the linkage to the obstacle, due to the geometric symmetry of the spherical shell.

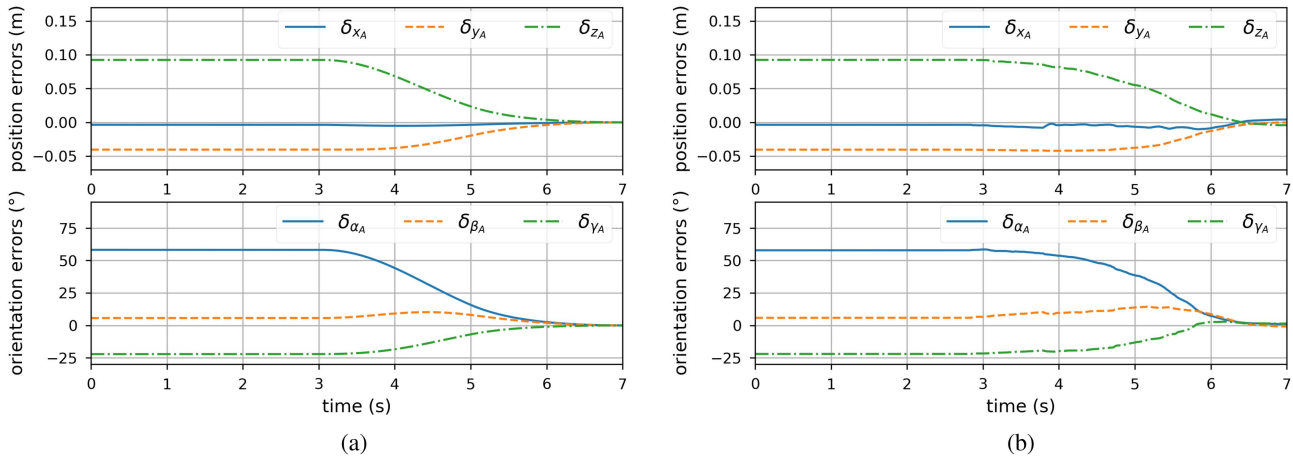

Fig. 13. Position and orientation errors of the end-effector for reaching the target pose A. (a) Simulation. (b) Experiment.

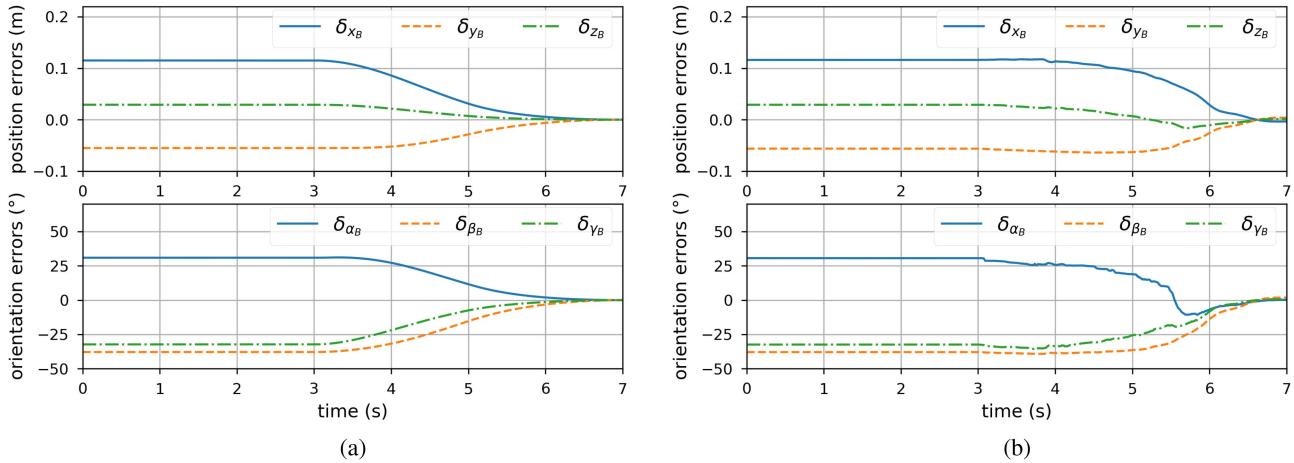

Fig. 14. Position and orientation errors of the end-effector for reaching the target pose B. (a) Simulation. (b) Experiment.

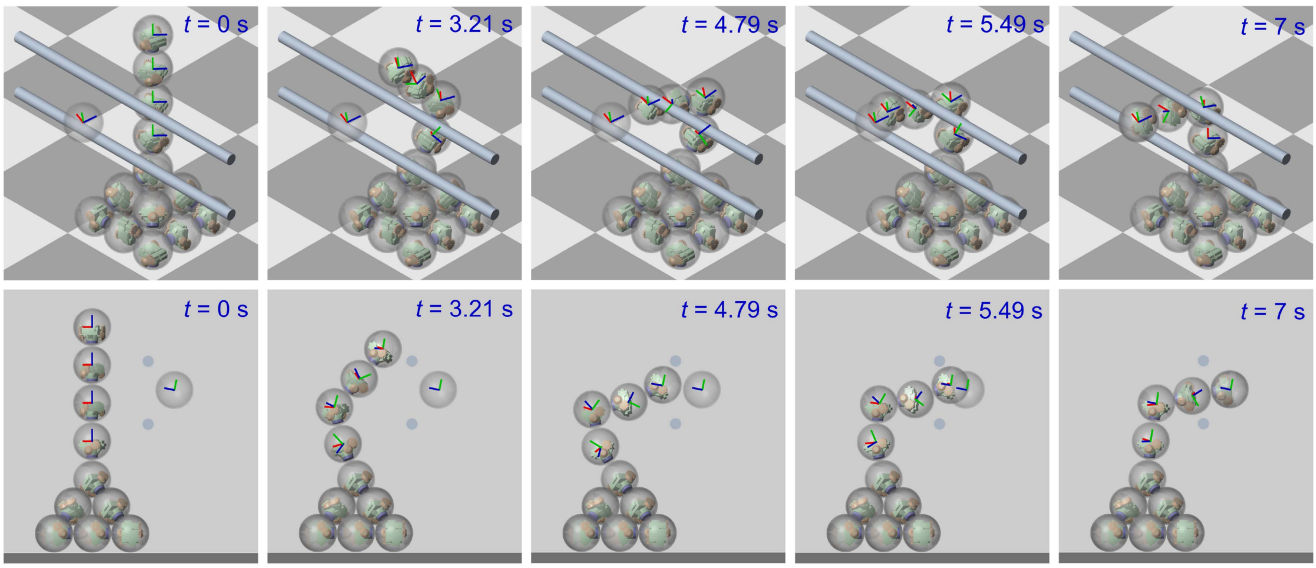

Fig. 15. Motion frames of the eight-DOF SRC joint manipulator reaching the target pose with obstacle avoidance.

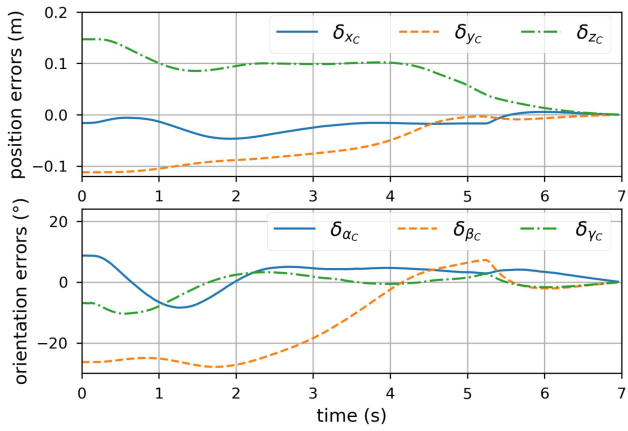

Fig. 16. Position and orientation errors of the end-effector for reaching the target pose C.

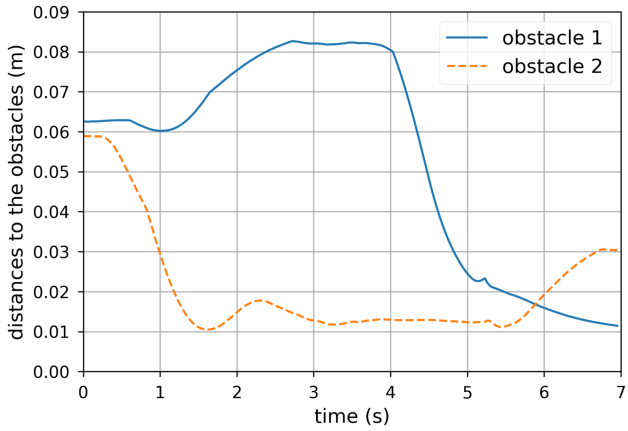

Fig. 17. Closest distances between the SRC joint manipulator and obstacles.

The position and orientation deviations of the end-effector during the whole movement are shown in Fig. 16, and the closest distances on the manipulator to the obstacles are shown in Fig. 17. It can be seen that the target pose is reached accurately, and the distances to the obstacles are always greater than the set safety distance of 0.01 m, which validates the performance of the SRC joint manipulator in performing tasks in narrow spaces with obstacles.

VI. Conclusion

RC joints have attracted interests in the field of robotics. This article first proposed a novel two-DOF SRC joint, with its joint model being formulated thoroughly. Then, a serial manipulator formed by the two-DOF SRC joint, termed as the SRC joint manipulator, was presented, whose forward kinematics were established based on the two-DOF SRC joint model. The Jacobian matrix that relates the SRC joint velocity and the end-effector velocity was obtained, and the IK was solved using the adaptive DLS method. The FreeBOT was used to implement the motions of the two-DOF SRC joint and manipulator, where the path planning and control methods, including the velocity/position planning as well as forward- and steering-dependent/independent control, for the driving trolley were proposed. As a result, the SRC joint and manipulator can generate the reference velocities and reach the target positions. In addition, a physics simulation platform FreeBOT-SIM and a real manipulator composed of FreeBOTs were built for the SRC joint and manipulator, on which the SRC joint model, the kinematics of the SRC joint manipulator, and the path planning and control methods of the FreeBOTs were validated, through performing SRC joint motions as well as the tasks of the manipulator reaching target poses in a free or obstructed space. In future applications, the SRC joint manipulator could work in the environments with obstacles or narrow spaces, for example, embedded pipes in buildings and truss mechanisms for some infrastructure, using the geometric symmetry advantage of its spherical units. Motion planning of the SRC joint manipulator performing tasks in narrow and cluttered environments with complex obstacles will be further studied in future work.

Appendix A
Derivations in the SRC Joint Modeling

A. Angle–Axis Relationships Between the Bodies B_i and B_{i-1} Relative to the Tangent Plane P_i

In the inertial frame, since the bodies B_i and B_{i-1} have the same linear velocity at the contact point, one has

$$l_i\dot{\theta}_i = l_{i-1}\dot{\theta}_{i-1} \tag{68}$$

where $\dot{\theta}_i$ and $\dot{\theta}_{i-1}$ are rotation speeds of B_i and B_{i-1} relative to the inertial frame, respectively. The rotation speed of the tangent plane P_i satisfies the relationship

$$\dot{\theta}_{p_i} = \dot{\theta}_i - \dot{\theta}_{i-1} \tag{69}$$

The rotation speeds of B_i and B_{i-1} relative to the dynamic tangent plane P_i satisfy

$$\begin{cases} \dot{\theta}_{i,1} = \dot{\theta}_i - \dot{\theta}_{p_i} \\ \dot{\theta}_{i-1,2} = \dot{\theta}_{i-1} + \dot{\theta}_{p_i} \end{cases}. \tag{70}$$

Substituting (69) into (70) results in

$$\frac{\dot{\theta}_{i,1}}{\dot{\theta}_{i-1,2}} = \frac{\dot{\theta}_{i-1}}{\dot{\theta}_i} = \frac{l_i}{l_{i-1}}. \tag{71}$$

B. Conversion Between Angle–Axis and Quaternion Representations

The angular displacement of $\Delta\boldsymbol{q}_{i,1} = [\Delta\eta_{i,1}, \Delta\boldsymbol{\epsilon}_{i,1}]^\top \in \mathbb{R}^4$ is transformed into the angle–axis representation $\Delta\theta_{i,1}\hat{\boldsymbol{e}}_{i,1}$ using the relationship [8]

$$\begin{cases} \Delta\theta_{i,1} = 2\cos^{-1}(\Delta\eta_{i,1}) \\ \hat{\boldsymbol{e}}_{i,1} = \frac{\Delta\boldsymbol{\epsilon}_{i,1}}{\sin(\Delta\theta_{i,1}/2)} \end{cases}. \tag{72}$$

The unit quaternion representation of the angular displacement of $\sum B_{i-1}$ relative to $\sum P_i$, denoted as $\Delta\boldsymbol{q}_{i-1,2} = [\Delta\eta_{i-1,2}, \Delta\boldsymbol{\epsilon}_{i-1,2}]^\top \in \mathbb{R}^4$, can be calculated from $\Delta\theta_{i-1,2}\hat{\boldsymbol{e}}_{i-1,2}$

as follows:

$$\begin{cases}\Delta\eta_{i-1,2}=\cos\left(\Delta\theta_{i-1,2}/2\right)\\ \Delta\boldsymbol{\epsilon}_{i-1,2}=\hat{\boldsymbol{e}}_{i-1,2}\sin\left(\Delta\theta_{i-1,2}/2\right)\end{cases}. \tag{73}$$

C. Calculating Rotation Matrix From the Corresponding Unit Quaternion

The rotation matrix ${}^{B_{i-1}}\boldsymbol{R}_{B_i}$ is calculated from the unit quaternion $\boldsymbol{q}_i$, as shown in (74) shown at the bottom of this page [8].

Similar to (74), the rotation matrix ${}^{B_{i-1}}\boldsymbol{R}_{P_i}$ can be expressed as the functions of the unit quaternion $\boldsymbol{q}_{i-1,2}$ in (10), where

$$\boldsymbol{f}_1(\boldsymbol{q}_{i-1,2})=\begin{bmatrix}1-2\left(\boldsymbol{\epsilon}_{i-1,2}(2)^2+\boldsymbol{\epsilon}_{i-1,2}(3)^2\right)\\ 2\left(\boldsymbol{\epsilon}_{i-1,2}(1)\boldsymbol{\epsilon}_{i-1,2}(2)-\eta_{i-1,2}\boldsymbol{\epsilon}_{i-1,2}(3)\right)\\ 2\left(\boldsymbol{\epsilon}_{i-1,2}(1)\boldsymbol{\epsilon}_{i-1,2}(3)+\eta_{i-1,2}\boldsymbol{\epsilon}_{i-1,2}(2)\right)\end{bmatrix} \tag{75}$$

$$\boldsymbol{f}_2(\boldsymbol{q}_{i-1,2})=\begin{bmatrix}2\left(\boldsymbol{\epsilon}_{i-1,2}(1)\boldsymbol{\epsilon}_{i-1,2}(2)+\eta_{i-1}\boldsymbol{\epsilon}_{i-1,2}(3)\right)\\ 1-2\left(\boldsymbol{\epsilon}_{i-1,2}(1)^2+\boldsymbol{\epsilon}_{i-1,2}(3)^2\right)\\ 2\left(\boldsymbol{\epsilon}_{i-1,2}(2)\boldsymbol{\epsilon}_{i-1,2}(3)-\eta_{i-1,2}\boldsymbol{\epsilon}_{i-1,2}(1)\right)\end{bmatrix} \tag{76}$$

$$\boldsymbol{f}_3(\boldsymbol{q}_{i-1,2})=\begin{bmatrix}2\left(\boldsymbol{\epsilon}_{i-1,2}(1)\boldsymbol{\epsilon}_{i-1,2}(3)-\eta_{i-1,2}\boldsymbol{\epsilon}_{i-1,2}(2)\right)\\ 2\left(\boldsymbol{\epsilon}_{i-1,2}(2)\boldsymbol{\epsilon}_{i-1,2}(3)+\eta_{i-1,2}\boldsymbol{\epsilon}_{i-1,2}(1)\right)\\ 1-2\left(\boldsymbol{\epsilon}_{i-1,2}(1)^2+\boldsymbol{\epsilon}_{i-1,2}(2)^2\right)\end{bmatrix}. \tag{77}$$

D. Calculating Linear Velocity ${}^{B_{i-1}}_{B_{i-1}}\boldsymbol{v}_{B_i}$

$$\begin{aligned}{}^{B_{i-1}}_{B_{i-1}}\boldsymbol{v}_{B_i}&={}^{B_{i-1}}_{B_{i-1}}\boldsymbol{\omega}_{P_i}\times\left({}^{B_{i-1}}_{B_{i-1}}\boldsymbol{r}_{B_i}\right)\\ &=-\left({}^{B_{i-1}}\boldsymbol{R}_{P_i}\,{}^{B_{i-1}}_{P_i}\boldsymbol{r}_{B_i}\right)\times\left({}^{B_{i-1}}_{B_{i-1}}\boldsymbol{\omega}_{P_i}\right)\\ &=-\left({}^{B_{i-1}}\boldsymbol{R}_{P_i}\left[0,0,l_i+l_{i-1}\right]^\top\right)\times\left({}^{B_{i-1}}_{B_{i-1}}\boldsymbol{\omega}_{P_i}\right)\\ &=-(l_i+l_{i-1})\boldsymbol{f}_3^\times(\boldsymbol{q}_{i-1,2})\left({}^{B_{i-1}}_{B_{i-1}}\boldsymbol{\omega}_{P_i}\right)\\ &=(l_i+l_{i-1})\boldsymbol{f}_3^\times(\boldsymbol{q}_{i-1,2})\left({}^{P_i}_{B_{i-1}}\boldsymbol{\omega}_{B_{i-1}}\right).\end{aligned} \tag{78}$$

Appendix B
Derivations in the Manipulator Modeling

A. Iterative Process of Calculating ${}^{I}_{I}\boldsymbol{\omega}_{B_i}$

$$\begin{aligned}{}^{I}_{I}\boldsymbol{\omega}_{B_i}&={}^{I}\boldsymbol{R}_{B_{i-1}}\,{}^{B_{i-1}}_{B_{i-1}}\boldsymbol{\omega}_{B_i}+{}^{I}_{I}\boldsymbol{\omega}_{B_{i-1}}\\ &={}^{I}\boldsymbol{R}_{B_{i-1}}\,{}^{B_{i-1}}_{B_{i-1}}\boldsymbol{\omega}_{B_i}+{}^{I}\boldsymbol{R}_{B_{i-2}}\,{}^{B_{i-2}}_{B_{i-2}}\boldsymbol{\omega}_{B_{i-1}}+{}^{I}_{I}\boldsymbol{\omega}_{B_{i-2}}\\ &=\sum_{j=1}^{i}\left({}^{I}\boldsymbol{R}_{B_{j-1}}\,{}^{B_{j-1}}_{B_{j-1}}\boldsymbol{\omega}_{B_j}\right)+{}^{I}_{I}\boldsymbol{\omega}_{B_0}\\ &=\sum_{j=1}^{i}\left({}^{I}\boldsymbol{R}_{B_{j-1}}\boldsymbol{\Phi}_{j\boldsymbol{\omega}}\begin{bmatrix}{}^{B_{j-1}}_{P_j}\omega_{B_{jx}}\\ {}^{B_{j-1}}_{P_j}\omega_{B_{jy}}\end{bmatrix}\right)+{}^{I}_{I}\boldsymbol{\omega}_{B_0}.\end{aligned} \tag{79}$$

B. Calculating Linear Velocity ${}^{I}_{I}v_{B_i}$

Differentiating (26) results in

$$\begin{aligned}{}^{I}_{I}\boldsymbol{v}_{B_i}&={}^{I}_{I}\boldsymbol{v}_{B_0}+\sum_{j=1}^{i}\left({}^{I}_{I}\boldsymbol{\omega}^\times_{B_{j-1}}\,{}^{I}\boldsymbol{R}_{B_{j-1}}\,{}^{B_{j-1}}_{B_{j-1}}\boldsymbol{r}_{B_j}\right)\\ &\quad+\sum_{j=1}^{i}\left({}^{I}\boldsymbol{R}_{B_{j-1}}\,{}^{B_{j-1}}_{B_{j-1}}\boldsymbol{v}_{B_j}\right)\\ &={}^{I}_{I}\boldsymbol{v}_{B_0}-\sum_{j=1}^{i}\left({}^{B_{j-1}}_{I}\boldsymbol{r}^\times_{B_j}\,{}^{I}_{I}\boldsymbol{\omega}_{B_{j-1}}\right)\\ &\quad+\sum_{j=1}^{i}\left({}^{I}\boldsymbol{R}_{B_{j-1}}\,{}^{B_{j-1}}_{B_{j-1}}\boldsymbol{v}_{B_j}\right).\end{aligned} \tag{80}$$

Substituting (22) and (28) into (80) results in

$$\begin{aligned}{}^{I}_{I}\boldsymbol{v}_{B_i}&={}^{I}_{I}\boldsymbol{v}_{B_0}-\sum_{j=1}^{i}\left({}^{B_{j-1}}_{I}\boldsymbol{r}^\times_{B_j}\left({}^{I}_{I}\boldsymbol{\omega}_{B_0}+\boldsymbol{J}_{B_{j-1}\boldsymbol{\omega}}\,\boldsymbol{\omega}\right)\right)\\ &\quad+\sum_{j=1}^{i}\left({}^{I}\boldsymbol{R}_{B_{j-1}}\boldsymbol{\Phi}_{j\boldsymbol{v}}\begin{bmatrix}{}^{B_{j-1}}_{P_j}\omega_{B_{jx}}\\ {}^{B_{j-1}}_{P_j}\omega_{B_{jy}}\end{bmatrix}\right)\\ &={}^{I}_{I}\boldsymbol{v}_{B_0}-\sum_{j=1}^{i}\left({}^{B_{j-1}}_{I}\boldsymbol{r}^\times_{B_j}\right){}^{I}_{I}\boldsymbol{\omega}_{B_0}\\ &\quad-\sum_{j=1}^{i}\left({}^{B_{j-1}}_{I}\boldsymbol{r}^\times_{B_j}\boldsymbol{J}_{B_{j-1}\boldsymbol{\omega}}\right)\boldsymbol{\omega}+\boldsymbol{J}'_{B_i\boldsymbol{v}}\boldsymbol{\omega}\\ &={}^{I}_{I}\boldsymbol{v}_{B_0}+{}^{I}_{I}\boldsymbol{r}^\times_{0i}\,{}^{I}_{I}\boldsymbol{\omega}_{B_0}+\boldsymbol{J}_{B_i\boldsymbol{v}}\boldsymbol{\omega}\end{aligned} \tag{81}$$

where the expressions of ${}^{I}_{I}\boldsymbol{r}_{0i}$, $\boldsymbol{J}'_{B_i\boldsymbol{v}}$, and $\boldsymbol{J}_{B_i\boldsymbol{v}}$ are shown in (30)–(32), respectively.

Appendix C
Relationships Between the Trolley Forward and Steering Speeds and Wheel Speeds

As shown in Fig. 5(b) [8], wheel 1 and virtual wheel 2 have the same velocity at the tangent point c

$$r_{i,w}\frac{1}{2}(\omega_{ir}+\omega_{il})=r'_i\omega'_{ir} \tag{82}$$

$${}^{B_{i-1}}\boldsymbol{R}_{B_i}=\begin{bmatrix}1-2\left(\boldsymbol{\epsilon}_i(2)^2+\boldsymbol{\epsilon}_i(3)^2\right) & 2\left(\boldsymbol{\epsilon}_i(1)\boldsymbol{\epsilon}_i(2)-\eta_i\boldsymbol{\epsilon}_i(3)\right) & 2\left(\boldsymbol{\epsilon}_i(1)\boldsymbol{\epsilon}_i(3)+\eta_i\boldsymbol{\epsilon}_i(2)\right)\\ 2\left(\boldsymbol{\epsilon}_i(1)\boldsymbol{\epsilon}_i(2)+\eta_i\boldsymbol{\epsilon}_i(3)\right) & 1-2\left(\boldsymbol{\epsilon}_i(1)^2+\boldsymbol{\epsilon}_i(3)^2\right) & 2\left(\boldsymbol{\epsilon}_i(2)\boldsymbol{\epsilon}_i(3)-\eta_i\boldsymbol{\epsilon}_i(1)\right)\\ 2\left(\boldsymbol{\epsilon}_i(1)\boldsymbol{\epsilon}_i(3)-\eta_i\boldsymbol{\epsilon}_i(2)\right) & 2\left(\boldsymbol{\epsilon}_i(2)\boldsymbol{\epsilon}_i(3)+\eta_i\boldsymbol{\epsilon}_i(1)\right) & 1-2\left(\boldsymbol{\epsilon}_i(1)^2+\boldsymbol{\epsilon}_i(2)^2\right)\end{bmatrix}. \tag{74}$$

with

$$r_i' = \sqrt{r_{i,\text{in}}^2 - (l_{i,w}/2)^2}. \tag{83}$$

Therefore, one has

$$\omega_{ir}' = r_{i,w}\frac{1}{2}(\omega_{ir} + \omega_{il})/\sqrt{r_{i,\text{in}}^2 - (l_{i,w}/2)^2} \tag{84}$$

and

$$u_{if} = r_{i,\text{out}}\omega_{ir}' = \frac{r_{i,\text{out}}r_{i,w}}{\sqrt{r_{i,\text{in}}^2 - (l_{i,w}/2)^2}}\frac{1}{2}(\omega_{ir} + \omega_{il}). \tag{85}$$

For the rotation of the trolley, as shown in Fig. 5(a), one has

$$u_{is}\frac{l_{i,w}}{2} = \frac{\omega_{ir} - \omega_{il}}{2}r_{i,w} \tag{86}$$

which gives

$$u_{is} = \frac{r_{i,w}}{l_{i,w}}(\omega_{ir} - \omega_{il}). \tag{87}$$

REFERENCES

[1] S. Bhattacharya and S. K. Agrawal, "Spherical rolling robot: A design and motion planning studies," *IEEE Trans. Robot. Autom.*, vol. 16, no. 6, pp. 835–839, Dec. 2000.

[2] A. Cole, J. Hauser, and S. Sastry, "Kinematics and control of multifingered hands with rolling contact," in *Proc. IEEE Int. Conf. Robot. Autom.*, 1988, pp. 228–233.

[3] L. Cui and J. S. Dai, "A Darboux-frame-based formulation of spin-rolling motion of rigid objects with point contact," *IEEE Trans. Robot.*, vol. 26, no. 2, pp. 383–388, Apr. 2010.

[4] A. L. Jeanneau, J. Herder, T. Laliberté, and C. M. Gosselin, "A compliant rolling contact joint and its application in a 3-DOF planar parallel mechanism with kinematic analysis," in *Proc. Int. Des. Eng. Tech. Conf. Comput. Inf. Eng. Conf.*, 2004, vol. 46954, pp. 689–698.

[5] J. Kim, S. i. Kwon, Y. Moon, and K. Kim, "Cable-movable rolling joint to expand workspace under high external load in a hyper-redundant manipulator," *IEEE/ASME Trans. Mechatronics*, vol. 27, no. 1, pp. 501–512, Feb. 2022.

[6] Z. Li and J. Canny, "Motion of two rigid bodies with rolling constraint," *IEEE Trans. Robot. Autom.*, vol. 6, no. 1, pp. 62–72, Feb. 1990.

[7] K. Abe, K. Tadakuma, and R. Tadakuma, "ABENICS: Active ball joint mechanism with three-DoF based on spherical gear meshings," *IEEE Trans. Robot.*, vol. 37, no. 5, pp. 1806–1825, Oct. 2021.

[8] B. Siciliano and O. Khatib, *Springer Handbook of Robotics*. New York, NY, USA: Springer, 2016, pp. 13–31.

[9] L. Cui and J. S. Dai, "A polynomial formulation of inverse kinematics of rolling contact," *J. Mech. Robot.*, vol. 7, no. 4, 2015, Art. no. 041003.

[10] S. A. Tafrishi, M. Svinin, and M. Yamamoto, "Darboux-frame-based parametrization for a spin-rolling sphere on a plane: A nonlinear transformation of underactuated system to fully-actuated model," *Mech. Mach. Theory*, vol. 164, 2021, Art. no. 104415.

[11] C. L. Collins, "Kinematics of robot fingers with circular rolling contact joints," *J. Robot. Syst.*, vol. 20, no. 6, pp. 285–296, 2003.

[12] M. G. Catalano, G. Grioli, E. Farnioli, A. Serio, C. Piazza, and A. Bicchi, "Adaptive synergies for the design and control of the Pisa/IIT SoftHand," *Int. J. Robot. Res.*, vol. 33, no. 5, pp. 768–782, 2014.

[13] C. Della Santina, C. Piazza, G. Grioli, M. G. Catalano, and A. Bicchi, "Toward dexterous manipulation with augmented adaptive synergies: The Pisa/IIT SoftHand 2," *IEEE Trans. Robot.*, vol. 34, no. 5, pp. 1141–1156, Oct. 2018.

[14] H. Liu, K. Xu, B. Siciliano, and F. Ficuciello, "The MERO hand: A mechanically robust anthropomorphic prosthetic hand using novel compliant rolling contact joint," in *Proc. IEEE/ASME Int. Conf. Adv. Intell. Mechatronics*, 2019, pp. 126–132.

[15] S. W. Hong, J. Yoon, Y.-J. Kim, and H. S. Gong, "Novel implant design of the proximal interphalangeal joint using an optimized rolling contact joint mechanism," *J. Orthopaedic Surg. Res.*, vol. 14, no. 1, 2019, Art. no. 212.

[16] J. M. Boisclair, T. Laliberté, and C. Gosselin, "On the optimal design of underactuated fingers using rolling contact joints," *IEEE Robot. Autom. Lett.*, vol. 6, no. 3, pp. 4656–4663, Jul. 2021.

[17] C. L. Collins, "Kinematics of a spatial three degree-of-freedom robot with rolling contact joints," in *Proc. Int. Des. Eng. Tech. Conf./Comput. Inf. Eng. Conf.*, 2002, vol. 36533, pp. 447–453.

[18] J. M. You, H. Kim, J. Kim, and D.-S. Kwon, "Design and analysis of high-stiffness hyperredundant manipulator with sigma-shaped wire path and rolling joints," *IEEE Robot. Autom. Lett.*, vol. 6, no. 4, pp. 7357–7364, Oct. 2021.

[19] D. Zhang, Y. Sun, and T. C. Lueth, "Design of a novel tendon-driven manipulator structure based on monolithic compliant rolling-contact joint for minimally invasive surgery," *Int. J. Comput. Assist. Radiol. Surg.*, vol. 16, pp. 1615–1625, 2021.

[20] Y. Hu, L. Zhang, W. Li, and G.-Z. Yang, "Design and fabrication of a 3-D printed metallic flexible joint for snake-like surgical robot," *IEEE Robot. Autom. Lett.*, vol. 4, no. 2, pp. 1557–1563, Apr. 2019.

[21] P. Berthet-Rayne, K. Leibrandt, K. Kim, C. A. Seneci, J. Shang, and G.-Z. Yang, "Rolling-joint design optimization for tendon driven snake-like surgical robots," in *Proc. IEEE/RSJ Int. Conf. Intell. Robots Syst.*, 2018, pp. 4964–4971.

[22] D. H. Lee, M. Hwang, J. Kim, and D.-S. Kwon, "Payload optimization of surgical instruments with rolling joint mechanisms," in *Proc. IEEE/RSJ Int. Conf. Intell. Robots Syst.*, 2020, pp. 3131–3136.

[23] J. Beil and T. Asfour, "A rolling contact joint lower extremity exoskeleton knee," in *Proc. Int. Conf. Intell. Auton. Syst.*, 2018, pp. 263–277.

[24] N. Kimura and N. Iwatsuki, "Spatial rolling contact pair generating the specified relative motion between links," in *Mechanism and Machine Science*. New York, NY, USA: Springer, 2016, pp. 307–316.

[25] N. Kimura, N. Iwatsuki, and I. Ikeda, "Spatial rolling contact pair with a hybrid elastic constraint composed of flexible bands and linear springs," *Mech. Eng. J.*, vol. 6, no. 6, 2019, Art. no. 19-00253.

[26] N. Kimura, N. Iwatsuki, and I. Ikeda, "Development of the active spatial rolling contact pair to generate the specified trajectory," *Mech. Eng. J.*, vol. 8, no. 3, 2021, Art. no. 20-00475.

[27] G. Liang, H. Luo, M. Li, H. Qian, and T. L. Lam, "FreeBOT: A freeform modular self-reconfigurable robot with arbitrary connection point-design and implementation," in *Proc. IEEE/RSJ Int. Conf. Intell. Robots Syst.*, 2020, pp. 6506–6513.

[28] G. H. Golub and C. Reinsch, "Singular value decomposition and least squares solutions," in *Linear Algebra*. New York, NY, USA: Springer, 1971, pp. 134–151.

[29] S. Chiaverini, B. Siciliano, and O. Egeland, "Review of the damped least-squares inverse kinematics with experiments on an industrial robot manipulator," *IEEE Trans. Control Syst. Technol.*, vol. 2, no. 2, pp. 123–134, Jun. 1994.

[30] J. Santoso and C. D. Onal, "An origami continuum robot capable of precise motion through torsionally stiff body and smooth inverse kinematics," *Soft Robot.*, vol. 8, no. 4, pp. 371–386, 2021.

[31] S. Chiaverini and B. Siciliano, "The unit quaternion: A useful tool for inverse kinematics of robot manipulators," *Syst. Anal. Model. Simul.*, vol. 35, no. 1, pp. 45–60, 1999.

[32] M. Yim et al., "Modular self-reconfigurable robot systems," *IEEE Robot. Autom. Mag.*, vol. 14, no. 1, pp. 43–52, Mar. 2007.

[33] *Simscape Multibody*. Natick, MA, USA: MathWorks Inc., 2020. [Online]. Available: https://www.mathworks.com/products/simmechanics.html

[34] B. Faverjon and P. Tournassoud, "A local based approach for path planning of manipulators with a high number of degrees of freedom," in *Proc. IEEE Int. Conf. Robot. Autom.*, 1987, vol. 4, pp. 1152–1159.

[35] O. Kanoun, F. Lamiraux, and P. B. Wieber, "Kinematic control of redundant manipulators: Generalizing the task-priority framework to inequality task," *IEEE Trans. Robot.*, vol. 27, no. 4, pp. 785–792, Aug. 2011.

Lijun Zong (Member, IEEE) received the B.S. degree in detection, guidance, and control technology from the Beijing Institute of Technology, Beijing, China, in 2013, and the M.S. and Ph.D. degrees in flight vehicle design from Northwestern Polytechnical University, Xi'an, China, in 2015 and 2020, respectively.

He was cosupervised as a visiting Ph.D. student with the Institute for Aerospace Studies, University of Toronto, Toronto, ON, Canada, from 2016 to 2018. He is currently a Postdoctoral Fellow with the Chinese University of Hong Kong, Shenzhen, China, and the University of Science and Technology of China, Hefei, China. His research interests include space manipulators and modular self-reconfigurable robots.

Guanqi Liang (Student Member, IEEE) received the B.S. degree in electrical engineering and automation from the China University of Mining and Technology, Jiangsu, China, in 2019. He is currently working toward the Ph.D. degree with the Chinese University of Hong Kong, Shenzhen, China.

His main research interests include modular robotics and reconfigurable robotics.

Mr. Liang received the IROS Best Paper Award on Robot Mechanisms and Design in 2020.

Tin Lun Lam (Senior Member, IEEE) received the B.Eng. (First Class Hons.) and Ph.D. degrees in robotics and automation from the Chinese University of Hong Kong, Hong Kong, in 2006 and 2010, respectively.

He is currently an Assistant Professor with the Chinese University of Hong Kong, Shenzhen, China, the Executive Deputy Director of the National-Local Joint Engineering Laboratory of Robotics and Intelligent Manufacturing, and the Director of Center for the Intelligent Robots, Shenzhen Institute of Artificial Intelligence and Robotics for Society. He has authored or coauthored two monographs and more than 50 research papers in top-tier international journals and conference proceedings in robotics [IEEE TRANSACTIONS ON ROBOTICS, *Journal of Field Robotics*, IEEE/ASME TRANSACTIONS ON MECHATRONICS (T-MECH), IEEE ROBOTICS AND AUTOMATION LETTERS, IEEE International Conference on Robotics and Automation, and IEEE/RSJ International Conference on Intelligent Robots and Systems (IROS)]. He holds more than 70 patents. His research interests include multirobot systems, field robotics, and collaborative robotics.

Dr. Lam received an IEEE/ASME T-MECH Best Paper Award in 2011 and the IROS Best Paper Award on Robot Mechanisms and Design in 2020.